Aerospace Science and Technology 180 (2027) 113745

Contents lists available at ScienceDirect

Aerospace Science and Technology

journal homepage: www.elsevier.com/locate/aescte

Original article

# A variable-order accurate framework for finite-strain static aeroelastic analysis

Elisa Testaquatra, Vincenzo Gulizzi *

*Department of Engineering, Università degli Studi of Palermo, Viale delle Scienze, Building 8, 90128, Palermo, Italy*

ARTICLE INFO

Communicated by Dr Jiaqing Kou

*Keywords:*
Finite strain
Hyperelasticity
Discontinuous Galerkin method
Non-planar vortex lattice method
Nonlinear aeroelasticity

ABSTRACT

In this work, a novel computational framework for nonlinear elastic and aeroelastic analysis of highly flexible wings is presented. The proposed approach couples a discontinuous Galerkin (DG) formulation for finite-strain, total Lagrangian three-dimensional elasticity with a non-planar Vortex Lattice Method (VLM) for aerodynamic modeling. The structural formulation employs a variable-order approximation of the displacement field, allowing independent tuning of the accuracy along the three spatial directions. The aerodynamics is evaluated on the deformed configuration using a non-planar VLM, where the vortices location follows the large deformations of the wing structure. The DG-VLM coupling is achieved by considering the forces generated by the vortices as energetically equivalent body forces acting on the structure.

A series of numerical tests is performed to investigate the influence of the approximation order of the displacement field on the aeroelastic response of the analyzed wings. The obtained results show good agreement with analytical, numerical and experimental benchmark data, confirming the accuracy and robustness of the proposed framework and its potential as a valuable tool for capturing nonlinear aeroelastic effects in conceptual design.

## 1. Introduction

Over the last few decades, the study of high-aspect-ratio wings has gained significant attention, becoming crucial in the development of modern aircraft such as High-Altitude Long-Endurance (HALE) platforms. These vehicles, including unmanned aerial systems and solar powered aircraft, are widely employed in several missions, ranging from environmental monitoring and scientific research to airborne relays for telecommunications.

High-aspect-ratio wings are well known to improve aerodynamic efficiency and lower fuel consumption by reducing the induced drag. However, they also undergo large deformations and rotations, which can significantly affect their aerodynamic performances. The mutual interaction between structural flexibility and aerodynamic loads motivates the need for advanced methods and tools capable of predicting aeroelastic behaviors in the finite-strain regime [1].

Aeroelastic analysis of flexible structures has been extensively investigated both experimentally and numerically as analytical solutions are not available in general, especially if structural nonlinearities, such as large deformations and rotations, or fluid nonlinearities, such as shock waves, need to be considered.

From a structural model perspective, different beam models have been historically employed in the context of finite-strain aeroelasticity. For instance, the geometrically exact beam formulation [2] has been coupled with different approaches to the evaluation of the aerodynamic forces; examples include finite-state aerodynamics [3,4], solution of the Euler/Navier-Stokes equations via computational fluid dynamics (CFD) [5], and solution of potential-flow aerodynamics via the Vortex Lattice Method (VLM) [6]. The papers referenced above use displacements and rotations of the beam as primary degrees of freedom. Alternative approaches also exist, which are based on the use of strains [7–9] or strains and velocities [10,11] as primary variables. As an example, Su and Cesnik [8,9] evaluated the response of highly flexible wings by coupling a two-dimensional (2D) finite-state aerodynamic theory with a strain-based geometrically nonlinear beam formulation, whereby extensional strains, bending curvatures and twist curvatures are selected as independent degrees of freedom.

More recently, different models have been proposed to resolve the aeroelastic response of structures featuring complex geometries or pronounced three-dimensional deformation effects, for which beam-based structural models may require considerable effort to generate or even cease to be valid. Palacios and Cea [12] developed a condensation proce-

* Corresponding author.
*E-mail address:* vincenzo.gulizzi@unipa.it (V. Gulizzi).

https://doi.org/10.1016/j.ast.2026.113745
Received 1 April 2026; Received in revised form 21 July 2026; Accepted 3 September 2026
Available online 6 September 2026
1270-9638/© 2026 The Author(s). Published by Elsevier Masson SAS. This is an open access article under the CC BY license (http://creativecommons.org/licenses/by/4.0/).

**Nomenclature**

| | |
|---|---|
| $\boldsymbol{A}$, $A_{ij}$ | Aerodynamic coefficient matrix and its entries |
| $b/2$ | Wing semi-span |
| $\boldsymbol{B}$, $B_i$ | Aerodynamic right-hand-side vector and its entries |
| $\mathscr{B}^e$ | Boundary of the $e$th structural element |
| $c$ | Wing chord |
| $C_{ijkl}$ | Components of the elastic moduli tensor |
| $\mathscr{D}$, $\mathscr{D}^h$ | Wing domain and its representation as a collection of mesh elements |
| $\mathscr{D}^e$ | Domain of the $e$th structural element |
| $\mathbf{E}$, $E_{ij}$ | Green-Lagrange strain tensor and its components |
| $E$ | Young's modulus |
| $\mathbf{F}$, $F_{ij}$ | Deformation gradient tensor and its components |
| $\boldsymbol{F}_{\mathsf{A}}$ | Discrete force vector due to aerodynamic loads |
| $\boldsymbol{F}_{\mathsf{S}}$ | Discrete force vector due to structural loads |
| $h$ | Mesh size |
| $h_s$ | Thickness of the load-bearing cross-section |
| $\boldsymbol{H}$ | Discrete internal force vector |
| $\mathscr{I}^h$ | Set of inter-element interfaces |
| $I_1, I_2, I_3$ | Intervals defining the element volume along the wing chord, span and thickness |
| $\boldsymbol{J}$ | Deformation Jacobian |
| $\boldsymbol{\ell}^k$ | Leading-edge segment vector of the $k$th vortex |
| $N_e$ | Total number of structural mesh elements |
| $\boldsymbol{N}$, $N_i$ | Outward unit normal and its components |
| $N_Q$ | Total number of structural unknowns |
| $N_v$ | Total number of vortices |
| $N_\Gamma$ | Total number of aerodynamic unknowns |
| $\mathbf{P}$, $P_{ij}$ | First Piola-Kirchhoff stress tensor and its components |
| $P_k$ | Legendre polynomial of order $k$ |
| $\mathscr{P}^p$ | Space of polynomials of degree at most $p$ |
| $p_1, p_2, p_3$ | Approximation orders along wing chord, span and thickness |
| $\boldsymbol{Q}$, $Q^{ei}_{\alpha_1\alpha_2\alpha_3}$ | Vector of structural unknowns and its component |
| $\boldsymbol{t}$, $t_i$ | Traction vector and its components |
| $\boldsymbol{u}$, $u_i$ | Displacement vector and its components |
| $\boldsymbol{V}$ | Fluid velocity vector |
| $v_j$ | Test function for the equilibrium equation along the $j$th direction |
| $\mathscr{V}^{hp}$ | Space of discontinuous test/basis functions |
| $V_\infty$ | Free-stream velocity magnitude |
| $w$ | Strain energy density function |
| $w_s$ | Width of the load-bearing cross-section |
| $\alpha$ | Angle of attack |
| $\boldsymbol{\Gamma}$, $\Gamma_i$ | Vector of aerodynamic unknowns and its component |
| $\gamma_{ij}$ | Test function for the stress equation |
| $\delta_{ij}$ | Kronecker delta |
| $\delta(\boldsymbol{X})$ | Dirac delta function |
| $\mu$, $\mu_0$ | Penalty parameters |
| $\nu$ | Poisson's ratio |
| $\Pi_{ij}$ | Auxiliary symmetrization term for the discrete operator |
| $\rho_0$ | Material density in the reference configuration |
| $\rho_\infty$ | Free-stream fluid density |

*Acronyms*

| | |
|---|---|
| CFD | Computational Fluid Dynamics |
| DG | Discontinuous Galerkin |
| DLM | Doublet Lattice Method |
| EB | Euler–Bernoulli |
| FEM | Finite Element Method |
| MRM | Modal Rotation Method |
| VLM | Vortex Lattice Method |

dure, whereby the beam properties were computed from a linear three-dimensional (3D) finite element model; the approach was later extended to a geometrically nonlinear aeroelastic setting [13,14]. To improve the resolution of the chord-wise deformations, a nonlinear aeroelasticity framework based on the combined use of a corotational shell model and an unsteady vortex lattice formulation was developed by de Souza et al. [15] and by Tsushima et al. [16,17] to investigate the aeroelastic response of composite laminates and additively manufactured wings, respectively. The nonlinear aeroelastic characteristics of composite wings modeled by the corotational shell approach were also investigated by Qiao et al. [18] using a CFD solver rather than potential-flow aerodynamics. CFD was also employed in combination with a nonlinear shell model by Gray et al. [19] to develop an optimization framework for highly flexible wings. Ai et al. [20,21] modelled the free-play-induced nonlinear aeroelastic reponse of an all-movable horizontal tail by coupling the Doublet Lattice Method (DLM) and a 3D FEM of the structure. Medeiros et al. [22] presented a geometrically nonlinear reduced-order model based on the modal representation of a 3D structure and coupled to a CFD solver to study the aeroelastic response of high-aspect-ratio wings with complex structural configurations. A similar approach was proposed by Drachinsky and Raveh [23,24], who developed the Modal Rotation Method, a modal decomposition technique based on rotation modes rather than deformation modes; the method allows accounting for large-deformation nonlinearity using linear model data as input.

Besides the approaches described above, which use classical structural approximations, namely 1D beam models, 2D shell models and 3D models, a different class of numerical methods have also been developed in the literature for solving aeroelastic problems. These methods are based on a high-order approximation of the displacement fields throughout the structure domain and are usually referred to as high-order structural models. As a few examples, Varello et al. [25] and Carrera et al. [26] coupled high-order beam models with a planar VLM for static aeroelastic analysis for isotropic and orthotropic wings, respectively, showing the benefit of an enriched representation of the displacement fields throughout the beam cross-section. Gulizzi and Benedetti [27] developed a variable-order formulation for wings, whereby the order of approximation of the displacement components could be chosen independently along the chord, thickness and span directions; they coupled it with a non-planar VLM for static and flutter aeroelastic analysis of isotropic wings [27,28] and subsequently extended it to model multilayered composite plates [29,30], showing that, by changing the order of approximation, the formulation was able to recover the results of both beam-based and plate-based aeroelastic models available in commercial software libraries. Grifò et al. [31,32] coupled high-order equivalent plate models to a CFD software library to study static aeroelastic response in different aerodynamic regimes, including transonic flow. However, despite their potential, these higher-order structural models are limited to linear aeroelastic applications.

The aim of the present paper is then to fill this literature gap and develop a variable-order accurate framework for aeroelasticity in the finite-strain regime, assessing the effect of the order of approximation on the aeroelastic response of highly flexible wings. In addition, while the majority of the methods mentioned in the literature review solve the structural problem using the Finite Element Method (FEM), we propose the use of the discontinuous Galerkin (DG) formulation to solve the equations associated with the structural problem. DG methods are based on expressing the approximate displacement field using a space of discontinuous basis functions, and on enforcing solution continuity among adjacent elements and boundary conditions in a weak sense via suitably defined boundary integrals. The discontinuous nature of DG methods enables several interesting features in the field of computational modeling such as the use of generic spaces of approximations, which can also be different from element to element, since the continuity on the solution is not enforced by nodal equivalence but through said boundary integrals.

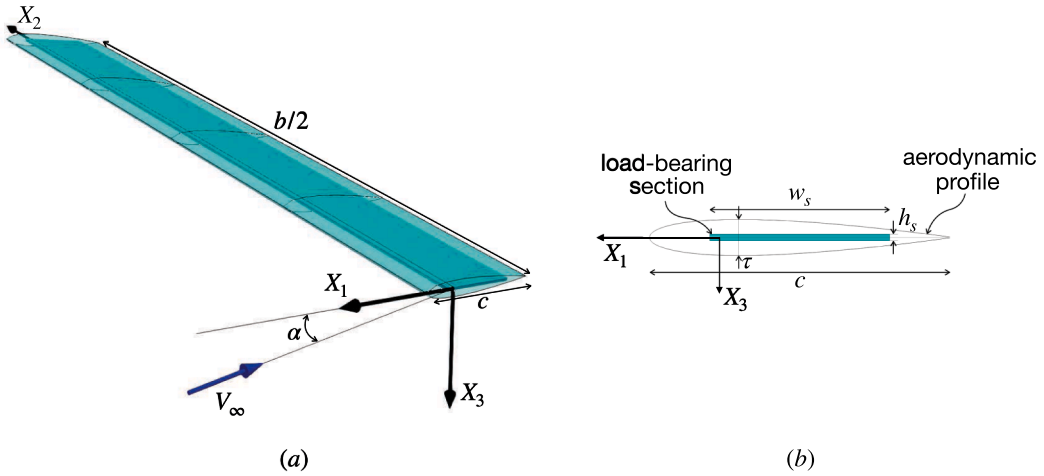


**Fig. 1.** (a) Wing geometry and free-stream flow condition. (b) Wing cross-section.

To solve the aeroelastic problems, the DG formulation is employed for solving the finite-strain 3D elastic response of the wing structures within a total Lagrangian settings, whereas the aerodynamics is resolved by a non-planar VLM, whose vortex lattice follows the deformation of the structure. The proposed framework has already been extensively validated in previous studies dealing with linear aeroelastic analysis of both isotropic [27,28] and multilayered composite wings [29,30]. The framework is extended to finite-strain regimes in the present work for the first time.

The paper is organized as follows: Section (2) describes the main geometrical features of the modelled wings, the governing equations of finite-strain elasticity, including the considered constitutive behavior, and hypothesis associated with the employed aerodynamic model. Section (3) introduces the developed computational framework for finite-strain static aeroelasticity: first, it presents the approach to discretizing the elasticity equation based on the discontinuous Galerkin method; second, it recalls the Vortex Lattice Method for solving the aerodynamic problem, highlighting the main aspects related to finite-strain applications; third, it describes the coupling between the structural and the aerodynamic solvers. Section (4) details the elastic and aeroelastic numerical tests that are performed to validate the framework. Section (5) discusses potential directions of further research before the Conclusions given in Section (6).

## 2. Problem description

This section introduces the aeroelastic problem, including the wing geometry, material properties, flow conditions, and governing equations of finite-strain elasticity and aerodynamics.

### 2.1. Wing description

The considered aeroelastic problem of a high-aspect-ratio wing is displayed in Fig. (1). The wing is described in a global reference system $OX_1X_2X_3$, which is centered at the quarter-chord point of the root section and is oriented such that: the axis $X_1$ is aligned with the chordwise direction and points towards the wing leading edge; the axis $X_3$ is orthogonal to the axis $X_1$, so that the $X_1X_3$ plane lies on the plane of the wing root cross-section; the axis $X_2$ is orthogonal to the $X_1X_3$ plane and is oriented so as to form a right-handed coordinate system. The half-span and the chord of the wing are denoted by $b/2$ and $c$, respectively, whereas the load-bearing cross-section consists of a rectangle of width $w_s$ and thickness $h_s$, as shown in Fig. (1b), and is made of an isotropic material characterized by Young's modulus $E$, Poisson's ratio $\nu$, and density $\rho_0$ in the reference, undeformed configuration. The location of the load-bearing cross-section with respect to the coordinate system depends on the considered problem and will be provided in Section (4) when the numerical results are discussed. Eventually, the wing is subject to a free-stream flow with magnitude $V_\infty$, angle of attack $\alpha$, and fluid density $\rho_\infty$.

### 2.2. Structural model

The considered wing structure is assumed to undergo large deformations and rotations. To describe its mechanical response, let us introduce the displacement field $\boldsymbol{u} \equiv (u_1, u_2, u_3)$ and the associated deformation gradient tensor $\mathbf{F}$, whose $ij$th component $F_{ij}$ is given as

$$F_{ij} \equiv \delta_{ij} + \frac{\partial u_i}{\partial X_j} \tag{1}$$

where $\delta_{ij}$ is the Kronecker delta function and $i, j \in \{1, 2, 3\}$. Additionally, let the material behavior be hyperelastic, i.e., be path independent and nondissipative, such that the stress state within the solid can be derived from a strain energy density function $w$, which, due to the principle of frame indifference, depends on the deformation gradient tensor $\mathbf{F}$ as $w = w(\mathbf{E})$, where $\mathbf{E} \equiv (\mathbf{F}^\intercal\mathbf{F} - \mathbf{I})/2$ is the Green-Lagrange strain tensor [33]. Then, considering a total Lagrangian description [33,34], the equilibrium equations governing the elastic response of the wing structure are written as follows

$$-\frac{\partial P_{ij}}{\partial X_i} - f_{0j} = 0 \tag{2}$$

where $f_{0j}$ is the $j$th component of the vector of body forces per unit volume in the reference configuration and $P_{ij}$ is the $ij$th component of the first Piola-Kirchhoff stress tensor $\mathbf{P}$, which is obtained from the strain energy density function $w$ as

$$P_{ij} = \frac{\partial w}{\partial E_{ik}} F_{jk}. \tag{3}$$

In Eqs. (2) and (3), and in the continuation of the paper, when the symbols $i$, $j$, and $k$ appear as repeated subscripts, they imply a summation over the three spatial dimensions.

The system of equations given in Eq. (2) must be supplemented with suitable boundary conditions (BCs). For the scope of the present work, zero-displacement BCs are assumed at the root of the wing structure, i.e., for the wing section at $X_2 = 0$, while the remaining boundaries of the wing are assumed traction-free. It is worth noting that the aerodynamic forces are evaluated within the hypothesis of potential-flow aerodynamics using the VLM, and will be applied to the wing structure as body forces entering Eq. (2).

The details of the numerical solution approach to the finite-strain elasticity equations are given in Section (3.1), where the aeroelastic coupling is discussed in Section (3.3).

#### 2.2.1. Constitutive behavior

The constitutive behavior of the wing structure is determined by the explicit expression of the strain energy function $w = w(\mathbf{E})$ introduced in the preceding section. Assuming a Saint Venant–Kirchhoff material model [33], the function $w$ has the following expression

$$w(\mathbf{E}) = \frac{1}{2} C_{ijkl} E_{ij} E_{kl}, \tag{4}$$

where $E_{ij}$ is the $ij$th component of the Green-Lagrange strain tensor $\mathbf{E}$ and $C_{ijkl}$ are the elastic moduli. Within the hypothesis of the considered material model, the elastic moduli coincide with those of the linear-elastic stress-strain law, whose associated strain energy function can be written as in Eq. (4) where the Green-Lagrange strain tensor components are replaced by the small-strain tensor components.

#### 2.2.2. Linear elasticity

The case of linear-elasticity is included in the governing equations described in the preceding sections. In particular, when the deformations and rotations are small, it is possible to show that the undeformed and deformed configurations are approximately coincident, the Green-Lagrange strain tensor approximately coincides with the small-strain tensor, and the first Piola-Kirchhoff stress tensor approximately coincides with the Cauchy stress tensor classically employed in linear elastic analysis.

### 2.3. Aerodynamic model

The considered approach to the modeling of the aerodynamic field is based on the theory of potential-flow aerodynamics, where the fluid flow can be considered inviscid, incompressible, and irrotational [35, 36]. In such a case, it is possible to show that the problem reduces to the solution of the Laplace equations over the fluid domain in combination with the impenetrability conditions defined on the solid boundary.

With regards to the fluid-structure interaction applications considered in this research study, the underlying hypothesis of potential-flow aerodynamics can be considered valid for low-Mach, high-Reynolds, attached flow over the wing structure.

The numerical solution of the aerodynamics problem is detailed in Section (3.2).

## 3. Computational framework

The computational framework developed in this paper is based on: *i*) the solution of the finite-strain elasticity problem via a variable-order accurate discontinuous Galerkin formulation, *ii*) the solution of the aerodynamic problem via the Vortex Lattice Method, and *iii*) a suitable coupling between these two numerical methods for aeroelastic analysis. Each of these elements is described in the following sections.

### 3.1. Discontinuous Galerkin formulation

The set of equations governing the elasticity problem discussed in Section (2.2) are numerically solved by employing a variable-order accurate discontinuous Galerkin formulation. The formulation has been presented and validated in previous studies regarding the static and dynamic response of beams [27,37], plates [29,30] and shells [38] in the linear elastic regime. In this research study, it is extended for the first time to account for finite-strain aeroelastic behaviors of flexible wing structures.

Similar to FEM, the DG method is based on the partition of the solid domain $\mathscr{D}$ into a collection of non-overlapping elements, i.e., $\mathscr{D} \approx \mathscr{D}^h = \bigcup_{e=1}^{N_e} \mathscr{D}^e$, where $\mathscr{D}^h$ denotes the approximate domain associated with the meshing procedure, $\mathscr{D}^e$ is the generic $e$th element, and

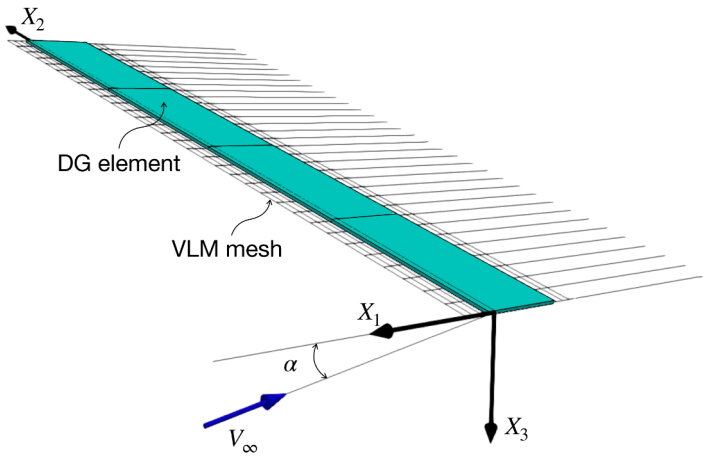


**Fig. 2.** Structural and aerodynamic discretization of the wing structure shown in Fig. (1).

$N_e$ is the total number of elements. However, unlike FEM, the Dirichlet BCs and the continuity of the solution among adjacent elements are not enforced by node equivalence, but they are fulfilled in a weak sense via boundary integrals suitably defined at the domain boundaries and at the inter-element interfaces. Such a discontinuous representation of the solution enables greater flexibility in the choice of the set of test and trial functions, which can be easily adapted to the needs of the problem at hand, different from element to element, and/or involving polynomials as well as non-polynomials approximation spaces [39]. As an example, Fig. (2) shows the four-element discretization of the load-bearing structure of the wing shown in Fig. (1).

Prior to providing the explicit expression of the approximate displacement field employed within the present DG framework, the DG weak statement of the considered elasticity problem will be obtained via following steps: *i*) first, Eqs. (2) and (3) are expressed in a weak sense over each element, *ii*) second, suitably defined boundary terms are introduced to link the solution among adjacent elements and to enforce the boundary conditions, *iii*) third, the weak statements of Eqs. (2) and (3) are combined and summed over all the mesh elements. The details are provided below.

Let $\mathcal{V}^{hp}$ be the space of discontinuous functions associated with the meshed domain $\mathscr{D}^h$ such that the generic function $v \in \mathcal{V}^{hp}$ is a polynomial of degree at most $p$ when restricted to each mesh element; compactly, $\mathcal{V}^{hp}$ is defined as follows

$$\mathcal{V}^{hp} \equiv \{v : \mathscr{D}^h \to \mathbb{R} \mid v(\boldsymbol{X} \in \mathscr{D}^e) \in \mathscr{P}^p(\mathscr{D}^e),\ \forall e = 1, \dots, N_e\}, \tag{5}$$

where $\mathscr{P}^p(\mathscr{D}^e)$ is the space of polynomials of degree at most $p$ defined over the $e$th element.

As customary in a Galerkin approach, the weak statement associated with the equilibrium equations along the $j$th direction is obtained by multiplying Eq. (2) by a test function $v_j \in \mathcal{V}^{hp}$, integrating over the generic mesh element $\mathscr{D}^e$, and performing integration by parts, which lead to

$$\int_{\mathscr{D}^e} \frac{\partial v_j}{\partial X_i} P^h_{ij} \mathrm{d}V - \int_{\mathscr{B}^e} v_j N_i \widehat{P}_{ij} \mathrm{d}S - \int_{\mathscr{D}^e} v_j f_{0j} \mathrm{d}V = 0, \tag{6}$$

where $\mathscr{B}^e$ denotes the boundary of the $e$th element, $N_i$ is the outer unit normal at $\mathscr{B}^e$, and $\widehat{P}_{ij}$ is the so-called *numerical flux* [40] of $P_{ij}$, i.e., an approximation to $P_{ij}$ on $\mathscr{B}^e$. Similarly, Eq. (3), i.e., the expression of the $ij$th component of the first Piola-Kirchhoff stress tensor, is multiplied by the test function $\gamma_{ij} \in \mathcal{V}^{hp}$, and the associated weak form reads

$$\int_{\mathscr{D}^e} \gamma_{ij} P^h_{ij} \mathrm{d}V = \int_{\mathscr{D}^e} \gamma_{ij} \frac{\partial w}{\partial E^h_{ik}} F^h_{jk} \mathrm{d}V + \int_{\mathscr{B}^e} N_i \Pi_{ij} (\widehat{u}_j - u^h_j) \mathrm{d}S, \tag{7}$$

where $\widehat{u}_i$ is the numerical flux of $u_i$ on $\mathscr{B}^e$, and the boundary integral appearing on the right-hand of the equation and involving the term $\Pi_{ij}$

has been added to render the tangent operator of the discrete problem symmetric [40].

In Eqs. (6) and (7), the superscript $h$ identifies approximate quantities introduced by the numerical method. For example, $u_j^h$ is the approximate $j$th component of the displacement field and $F_{jk}^h$ denotes the approximation of $F_{jk}$ computed by plugging $u_j^h$ into Eq. (1). On the other hand, the explicit expressions of the numerical fluxes $\widehat{P}_{ij}$ and $\widehat{u}_j$ depend on the type of boundary conditions, if $\mathscr{B}^e$ belongs to the domain boundary, or interface conditions, if $\mathscr{B}^e$ is shared by two adjacent elements, to be enforced. As the present formulation falls within the class of Interior Penalty discontinuous Galerkin methods [40], the following numerical fluxes are considered

$$\widehat{u}_i \equiv \begin{cases} \{u^h\} & \text{on } \mathscr{I}^h \\ \overline{u}_i & \text{on } \mathscr{B}_D^h \\ u_i^h & \text{on } \mathscr{B}_N^h \end{cases} \quad \text{and} \quad \begin{cases} \widehat{P}_{ij} \equiv \{\frac{\partial w}{\partial E_{ik}^h} F_{jk}^h\} - \mu [\![u_j^h]\!]_i & \text{on } \mathscr{I}^h \\ \widehat{P}_{ij} \equiv \frac{\partial w}{\partial E_{ik}^h} F_{jk}^h - \mu (u_j^h - \overline{u}_j) N_i & \text{on } \mathscr{B}_D^h \\ N_i \widehat{P}_{ij} \equiv \overline{t}_j & \text{on } \mathscr{B}_N^h \end{cases} \tag{8}$$

where: $\mathscr{I}^h$, $\mathscr{B}_D^h$, and $\mathscr{B}_N^h$ denote the collections of all elements boundaries where solution continuity, Dirichlet BCs, and Neumann BCs, respectively, are to be enforced; $\overline{u}_i$ denotes the prescribed values of the $i$th displacement component while $\overline{t}_i$ denotes the prescribed values of the $i$th traction component; $\mu$ is a *penalty parameter* chosen proportional to the ratio between the Young modulus $E$ and the mesh size $h$, i.e., $\mu \sim E/h$, in accordance with the theoretical predictions of Ref. [40] in the context of linear elliptic problems and the results obtained in Ref. [41] in the context of finite-strain elasticity; the operators $\{\bullet\}$ and $[\![\bullet]\!]_i$ are the so-called average and jump operators, respectively, which defined at the interface between two adjacent elements $e$ and $e'$ as follows

$$\{\bullet\} \equiv \frac{1}{2}(\bullet^e + \bullet^{e'}) \quad \text{and} \quad [\![\bullet]\!]_i \equiv \bullet^e N_i^e + \bullet^{e'} N_i^{e'}. \tag{9}$$

Eventually, Eqs. (6) and (7) are combined by setting $\gamma_{ij} \equiv \partial v_j / \partial X_i$ and substituting the leftmost term of Eq. (6) with the right-hand side of Eq. (7). Then, upon using the expression of the numerical fluxes given in Eq. (8) and summing over all the mesh elements, the DG weak statement of the elastic problem for the entire solid domain reads: find the approximate displacement field $\boldsymbol{u}^h$ with component $u_j^h \in \mathcal{V}^{hp}$ such that the following equality holds

$$\begin{aligned} &\int_{\mathscr{D}^h} \frac{\partial v_j}{\partial X_i} \frac{\partial w}{\partial E_{ik}^h} F_{jk}^h \mathrm{d}V - \int_{\mathscr{I}^h} \left( [\![v_j]\!]_i \left\{ \frac{\partial w}{\partial E_{ik}^h} F_{jk}^h \right\} + \{\Pi_{ij}\} [\![u_j^h]\!]_i \right) \mathrm{d}S \\ &\quad + \int_{\mathscr{I}^h} \mu [\![v_j^h]\!]_i [\![u_j^h]\!]_i \mathrm{d}S + \\ &\quad - \int_{\mathscr{B}_D^h} \left( v_j N_i \frac{\partial w}{\partial E_{ik}^h} F_{jk}^h + N_i \Pi_{ij} u_j^h \right) \mathrm{d}S + \int_{\mathscr{B}_D^h} \mu v_j^h u_j^h \mathrm{d}S = \\ &\quad = \int_{\mathscr{D}^h} v_j f_{0j} \mathrm{d}V + \int_{\mathscr{B}_N^h} v_j \overline{t}_j \mathrm{d}S - \int_{\mathscr{B}_D^h} N_i \Pi_{ij} \overline{u}_j \mathrm{d}S \\ &\quad + \int_{\mathscr{B}_D^h} \mu v_j \overline{u}_j \mathrm{d}S \end{aligned} \tag{10}$$

for any $v_j \in \mathcal{V}^{hp}$. A few comments regarding Eq. (10) are in order:

- The integrals appearing in Eq. (10) are usually referred to as *broken integrals* and implicitly denote a summation over the mesh elements or the mesh boundaries; for example,

$$\int_{\mathscr{D}^h} \bullet \, \mathrm{d}V \equiv \sum_{e=1}^{N_e} \int_{\mathscr{D}^e} \bullet^e \mathrm{d}V, \quad \int_{\mathscr{B}_D^h} \bullet \, \mathrm{d}S \equiv \sum_{e=1}^{N_e} \int_{\mathscr{B}_D^e} \bullet^e \mathrm{d}S, \tag{11}$$

  where $\mathscr{B}_D^e$ is the part of the $e$th element boundary where Dirichlet BCs are prescribed.
- The terms $\overline{u}_j$ and $\overline{t}_j$ have been included in the weak form for the sake of completeness in case non-zero Dirichlet BCs or non-zero Neumann BCs were to be considered. However, as already mentioned in Section (2.2), the wing is clamped at $X_2 = 0$ and its remaining boundaries are traction-free; therefore, $\overline{u}_j = 0$ on $\mathscr{B}_D^h$ and $\overline{t}_j = 0$ on $\mathscr{B}_N^h$, and the three rightmost integral on the right-hand side of Eq. (10) are zero for the considered aeroelastic problems.
- The aerodynamic forces acting on the structure are considered as energetically equivalent body forces via the leftmost integral on the right-hand side of Eq. (10). Their explicit expression is given in Section (3.2).
- The leftmost term on the left-hand side of Eq. (10) represents the internal work of the deforming body, while the two leftmost terms on the right-hand side represent the applied body forces and surface tractions; these terms are also found in a continuous Galerkin formulation. On the other hand, the boundary integrals over the collection $\mathscr{I}^h$ of inter-element interfaces and the collection $\mathscr{B}_D^h$ of element boundaries where Dirichlet BCs are enforced represent the additional terms that distinguish the discontinuous Galerkin formulation from a continuous Galerkin formulation such as FEM. They are required to ensure (in a weak sense) continuity of the solution as well as the enforcement of the Dirichlet BCs regardless of the choice of the approximation space.

The last aspect of the proposed formulation concerns the approximation of the displacement field throughout the wing structure. Considering that the analyzed wings are divided into elements along their span such that the generic structural element occupies the volume $\mathscr{D}^e = I_1 \times I_2 \times I_3$, with $I_1 \equiv [-3c/4, c/4]$, $I_2 \equiv [(e-1)h, eh]$, $I_3 \equiv [-h_s/2, h_s/2]$, being $h = b/(2N_e)$ and $e = 1, \dots, N_e$, the expression of the $i$th component $u_i^h$ over the $e$th element is given in the space of tensor-product Legendre polynomials as

$$u_i^h(\boldsymbol{X} \in \mathscr{D}^e) = \sum_{\alpha_1=0}^{p_1} \sum_{\alpha_2=0}^{p_2} \sum_{\alpha_3=0}^{p_3} P_{\alpha_1}(X_1) P_{\alpha_2}(X_2) P_{\alpha_3}(X_3) Q_{\alpha_1\alpha_2\alpha_3}^{ei}, \tag{12}$$

where $P_k(X_i)$ is the Legendre polynomial of order $k$ of the spatial coordinate $X_i$ scaled in the interval $I_i$, $Q_{\alpha_1\alpha_2\alpha_3}^{ei}$ denotes the unknown series coefficient associated with a polynomial of order $\alpha_1$ along the chord, $\alpha_2$ along the span, and $\alpha_3$ along the thickness of the wing to be obtained by solving the discrete version of Eq. (10). Eventually, it is worth noting that $p_1$, $p_2$, and $p_3$ – the orders of approximation of the displacement field along the chord, span and thickness of the wing structure, respectively– can be independently selected along the three spatial directions.

### 3.2. Vortex lattice method

The aerodynamic interaction between the structure and the fluid is modeled under the assumptions of potential-flow aerodynamics and resolved by the Vortex Lattice Method [36]. As the VLM is a well-established technique, this section only briefly describes its main features in relation to the considered finite-strain aeroelasticity applications.

According to the VLM approach, the wing is represented as a lifting surface that is discretized into a collection of ring vortices, while its aerodynamic wake is represented by a set of horseshoe vortices shed by the wing trailing edge. An example of the VLM mesh of the wing shown in Fig. (1a) is displayed in Fig. (2).

The unknowns associated with the VLM approximation are the vortex strengths $\Gamma_k$, with $k = 1, \dots, N_v$, being $N_v$ the total number of vortices, that are obtained by imposing the aerodynamic impenetrability condition on the velocity field over the lifting surface [36], leading to a system of equations of the form

$$A_{ik} \Gamma_k = B_i, \tag{13}$$

where $i = 1, \dots, N_v$, $A_{ik}$ is the $ik$th entry of the aerodynamic coefficient matrix, and $B_i$ is the $i$th entry of the right-hand side. It is worth noting that both the terms $A_{ik}$ and the terms $B_i$ depend on the location of the vortices, which, in case of a highly deformable structure, depends on the displacement field and thus the unknowns of the structural problem.

Given the strength $\Gamma_k$ of the $k$th vortex, the aerodynamic force $\boldsymbol{f}^k = (f_1^k, f_2^k, f_3^k)$ generated by the same vortex on the wing structure

is computed as

$$\boldsymbol{f}^k = \rho_\infty \boldsymbol{V}^k \times \boldsymbol{\ell}^k \widetilde{\Gamma}_k \tag{14}$$

where $\boldsymbol{\ell}^k$ is the leading-edge segment vector of the deformed $k$th vortex, $\boldsymbol{V}^k$ is the fluid velocity computed at the midpoint of $\boldsymbol{\ell}^k$, and $\widetilde{\Gamma}_k$ is the net circulation at the leading-edge segment of the vortex, coinciding with $\Gamma_k$ if the $k$th vortex is at the leading edge of the wing, or given otherwise by the difference of the circulation strengths of two chord-wise contiguous vortexes. The aerodynamic forces are transferred onto the structure via the leftmost integral of the right-hand side of Eq. (10), where the aerodynamic contribution to the $j$th component $f_{0j}$ is evaluated as the sum of concentrated aerodynamic forces, i.e.,

$$f_{0j} = \sum_{k=1}^{N_v} \boldsymbol{J}^k f_j^k \delta(\boldsymbol{X} - \boldsymbol{X}^k), \tag{15}$$

where $\delta(\boldsymbol{X})$ is the Dirac delta function, $\boldsymbol{X}^k$ is the midpoint of the leading edge of the undeformed $k$th vortex, and $\boldsymbol{J}^k$ is the deformation Jacobian evaluated at $\boldsymbol{X}^k$.

### 3.3. Aeroelastic coupling

The coupling between the structural model and the aerodynamic model is twofold. On the one hand, the forces acting on the structure depend on the vortex strength of the aerodynamics problem; on the other hand, the location of the aerodynamic vortices depends on the deformation of the structure. More specifically, upon introducing the $N_Q$-dimensional vector $\boldsymbol{Q}$, being $N_Q$ the total number of structural unknowns, and the $N_\Gamma$-dimensional vector $\boldsymbol{\Gamma}$, being $N_\Gamma \equiv N_v$ the total number of aerodynamic unknowns, which coincides with the number of VLM vortices, the system of equations governing the aeroelastic problem can be written as follows:

$$\begin{cases} \boldsymbol{H}(\boldsymbol{Q}) = \boldsymbol{F}_{\mathsf{A}}(\boldsymbol{\Gamma}) + \boldsymbol{F}_{\mathsf{S}} \\ \boldsymbol{A}(\boldsymbol{Q})\boldsymbol{\Gamma} = \boldsymbol{B}(\boldsymbol{Q}) \end{cases} \tag{16}$$

where the top equation corresponds to the discrete version of DG weak statement discussed in Section (3.1) and obtained by plugging Eq. (12) into Eq. (10) and letting $v_j$ span the space of test functions, while the bottom equation corresponds to the discrete version of aerodynamic problem solved by the VLM as discussed in Section (3.2).

The system given in Eq. (16) highlights the aeroelastic coupling, as both equations depend on the structural and aerodynamic unknowns. In particular, the term $\boldsymbol{H}(\boldsymbol{Q})$ is a $N_Q$-dimensional vector that stems from the left-hand side of Eq. (10) and depends nonlinearly on $\boldsymbol{Q}$; $\boldsymbol{F}_{\mathsf{A}}(\boldsymbol{\Gamma})$ is the $N_Q$-dimensional vector stemming from the aerodynamic contribution to the right-hand side of Eq. (10); $\boldsymbol{F}_{\mathsf{S}}$ is the $N_Q$-dimensional vector that stems from the structural loads acting on the structure such as weight or concentrated forces; $\boldsymbol{A}(\boldsymbol{Q})$ is the $N_\Gamma \times N_\Gamma$ aerodynamic coefficient matrix whose entries depends on the location of the vortices and thus on $\boldsymbol{Q}$; $\boldsymbol{B}(\boldsymbol{Q})$ is the $N_\Gamma$-dimensional aerodynamic right-hand side whose entries depend on the free-stream velocity $V_\infty$ and the vortex locations.

The system of equations given in Eq. (16) is nonlinear in the unknowns $\boldsymbol{Q}$ and $\boldsymbol{\Gamma}$ and is solved iteratively for given values of free-stream velocity and structural loads using the Newton-Raphson approach.

## 4. Numerical results

In this section, the developed framework is numerically tested and validated against a wide set of computational and experimental tests available in the literature involving elastic and aeroelastic problems in the finite-strain regime. It is recalled that, in terms of boundary conditions, the considered structures are always clamped at $X_2 = 0$.

The variable-order capabilities of the framework are assessed by considering different orders of approximation of the displacement field as reported in Eq. (12). In particular, the analyses are performed by selecting different orders of approximation $p_1 = p_3 = p_c$ across the wing cross-section and order of approximation $p_2 = p_b$ along the wing span, and denoting the corresponding results by $\mathsf{DG}_{p_c p_b p_c}$. It is worth noting that the case $p_c = 1$ corresponds to a linear approximation of the displacement field across the wing cross-section, which is similar to the hypothesis generally employed for beam-based models. However, beam-based formulations do not consider the 3D stress-strain constitutive law but a suitably modified version of the elastic coefficients, introducing, for example, the shear factor, that renders the response of the modeled structure less stiff. In this study, when $p_c = 1$, the elastic coefficients are modified according to the procedure described in Ref. [29], and the corresponding results are identified $\mathsf{DG}_{1 p_b 1^*}$.

### 4.1. Nonlinear cantilever beam

The first considered test is the cantilever beam case analyzed in Ref. [42]. With reference to Fig. (1), the beam has a square cross-section with $h_s = w_s$ centered at $X_1 = 0$ and $X_3 = 0$, its length is denoted by $L \equiv b/2$, and is subjected to a concentrated load $P$ acting along the $X_3$ direction at $\boldsymbol{X} = (0, L, 0)$. The beam is made of an isotropic material characterized by Young's modulus $E = 75$ GPa and Poisson's ratio $\nu = 0.33$.

The elastic response of the beam is shown in Fig. (3) in terms of non-dimensional displacement $u_z/L$, with $u_z \equiv -u_3(0, L, 0)$, as a function of the non-dimensional load $PL^2/(EI)$, where $I$ is the bending moment of inertia of the cross-section. Two values of the beam slenderness $L/w_s$ are considered, namely $L/w_s = 10$ and $L/w_s = 100$, and the associated results are reported in Fig. (3a) and (b), respectively. The figures show the values of displacement $u_z/L$ obtained by the present framework using a five-element mesh and three different DG schemes, namely $\mathsf{DG}_{151^*}$, $\mathsf{DG}_{252}$, $\mathsf{DG}_{353}$. The figures also report the values obtained in Ref. [42], corresponding to the analytical solution of the nonlinear Euler-Bernoulli beam equation, and the values obtained in Ref. [43], corresponding to a FEM-based solution of a second-order beam model; in the figure, the former is labeled as Beam (EB) - analytic, while the latter is labeled as Beam (L9). In all cases, an excellent matching between the results obtained with the present formulation and the results available in the literature is observed. For the sake of completeness, the values of the tip displacement computed under the hypothesis of a linear-elastic behavior are reported in the figures, highlighting the importance of considering the nonlinear effects for sufficiently large values of the external load. Eventually, the insets in the figures display the deformed configuration to scale of the beams corresponding to $PL^2/(EI) = 7$.

The test is also employed to investigate the sensitivity of the formulation with respect to the chosen value of the penalty parameter $\mu$ discussed in Section (3.1) as well as the computational efficiency of the proposed methodology in terms of accuracy versus degrees of freedom and compute time.

First, upon defining the penalty parameter as $\mu = \mu_0 E/h$, with $h \equiv L/N_e$ and $N_e$ corresponding to the number of elements along the beam length, the response of the beam is computed for different values of the constant $\mu_0$. The obtained numerical results confirm that there exists a value of $\mu_0^{\min}$, approximately equal to 60 in this case, such that, for $\mu_0 < \mu_0^{\min}$, the numerical scheme does not converge for all values of the applied load due to a stagnating behavior of the residuals. On the other hand, for $\mu_0 > \mu_0^{\min}$, the computed solution converges within a few Newton-Raphson iterations and is insensitive to the value of the penalty parameter, as it can be seen from Fig. (4a) and (b), which report the values of $u_z/L$ as a function of $PL^2/(EI)$ for the case of the short beam ($L/w_s = 10$) and the case of the slender beam ($L/w_s = 100$), respectively, for different values of $\mu_0$. These observations are consistent with theoretical predictions [40] and literature results [41] that recommend choosing $\mu = \mu_0 E/h$ with $\mu_0 > \mu_0^{\min}$ sufficiently large; however, it is worth noting that the value of $\mu_0^{\min}$ may depend on the specific application. Throughout the paper, all numerical tests are obtained by setting $\mu_0 = 10^2$.

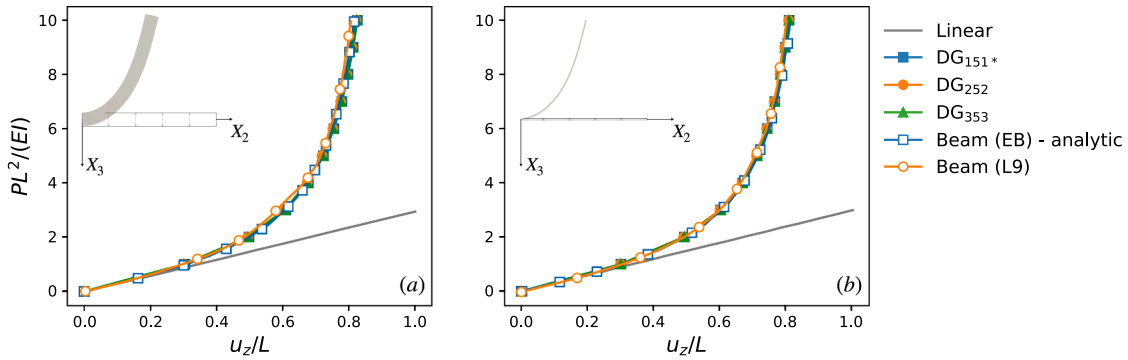


**Fig. 3.** Non-dimensional tip displacement $u_z/L$ as a function of the non-dimensional tip load $PL^2/EI$ for a cantilever beam with slenderness ratio (*a*) $L/w_s = 10$ and (*b*) $L/w_s = 100$.

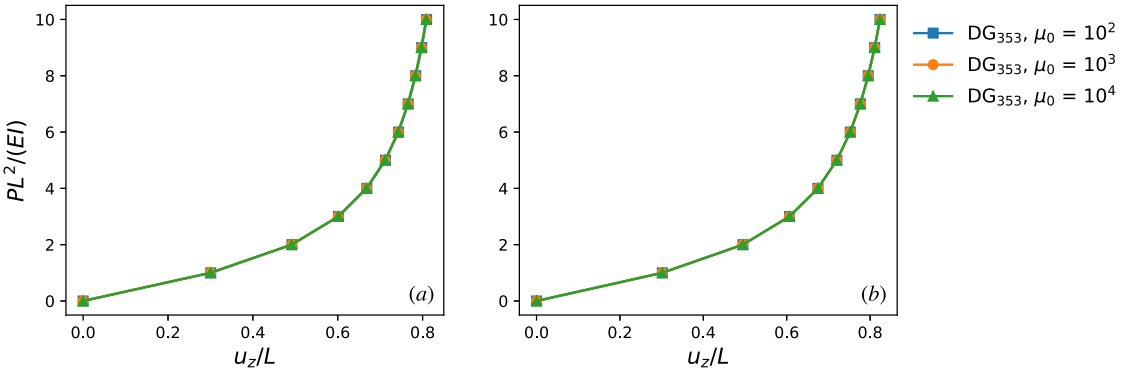


**Fig. 4.** Sensitivity of the response of the cantilever-beam problem with respect to the penalty constant $\mu_0$ for slenderness ratio (*a*) $L/w_s = 10$ and (*b*) $L/w_s = 100$.

Second, to assess the computational efficiency of the methodology, the following error measure is introduced

$$e(f) \equiv \frac{\max_{\mathscr{H}} |f - f^{\text{ref}}|}{\max_{\mathscr{H}} |f^{\text{ref}}|}, \tag{17}$$

where $f$ is a generic function (e.g., a displacement component), $f^{\text{ref}}$ is the associated reference solution, and $\mathscr{H}$ denotes the load history. Fig. (5a) and (b) show the error given in Eq. (17) with $f \equiv u_z$ for the short beam case as a function of the total number of degrees of freedom (DOF) and the compute time, respectively, obtained considering different polynomial approximations and a ten-element $\text{DG}_{555}$-scheme reference solution. Note that the total number of degrees of freedom corresponds to $\text{DOF} \equiv 3(1+p_c)^2(1+p_b)N_e$ whereas the compute time is the time needed by the code to solve the nonlinear system of equations for each value of the load $P$. A machine running Windows and featuring a 3.2GHz Intel(R) Core(TM) i9-14900KF processor and 128 GB of RAM has been employed for all numerical tests. It is also worth noting that the code is written mostly in Python, with a few routines written in Fortran.

In Fig. (5a) and (b), each curve corresponds to varying the number of span-wise mesh elements $N_e$ for a given set of cross-sectional and spanwise approximation orders. The solution obtained with two groups of DG schemes are reported in the figures: one group displayed with hollow markers uses the same order of approximation throughout the beam cross section and the beam length, i.e., $p_c = p_b$, with $p_c \in \{2,3,4,5\}$; the second group is displayed with filled markers and uses a mixed-order approach where $p_b = 5$ and $p_c \in \{1,2,3,4\}$. As expected for a beam-like structure, the results show that combining a mid-order cross-sectional approximation with a high-order spanwise approximation provides the most efficient discretization: for a given level of accuracy, such mixed-order schemes require fewer degrees of freedom and, more significantly, a shorter compute time than schemes employing the same order of approximation along the three spatial directions. It is worth noting that the error associated with the $\text{DG}_{151^*}$ scheme does not change with mesh refinement, pointing to the fact that the solution has reached its converged value, which however stays within 0.4% of the reference solution. Such a plateau behavior is explained considering that the $\text{DG}_{151^*}$ scheme uses a modified version of the stiffness coefficients as explained at the beginning of Section (4) in addition to the low-order cross-sectional representation of the solution.

A similar analysis is performed for the slender beam ($L/w_s = 100$). The error measure given in Eq. (17) is reported for different approximation orders as a function of DOF and as a function of the compute time in Fig. (6a) and (b), respectively, using the analytical solution of the nonlinear Euler-Bernoulli beam equation as the reference solution. Fig. (6a) also reports the error associated with the solution obtained using `NASTRAN` CBEAM elements, showing that the $\text{DG}_{151^*}$ scheme provides an error-vs-DOF behavior similar to that of the commercial software. Also in this case, a mixed-order of approximation performs better, in terms of error-vs-DOF and error-vs-compute time, than using the same order of approximation along the three spatial directions. Eventually, it is noted that the $\text{DG}_{151^*}$ scheme attains a lower error than the higher-order schemes since the employed reference solution is that of the Euler-Bernoulli beam equation, which is better reproduced by the beam-like kinematics of the $\text{DG}_{151^*}$ scheme and the CBEAM elements.

### 4.2. Elastic and aeroelastic analysis of the Pazy wing

In the second set of tests, the capability and accuracy of the developed framework are assessed considering the Pazy wing case [44,45], a recently proposed benchmark showing the effect of large deformations on the aeroelastic response of highly flexible wings. This test has been reproduced by several research groups [46,47] with the aim to compare

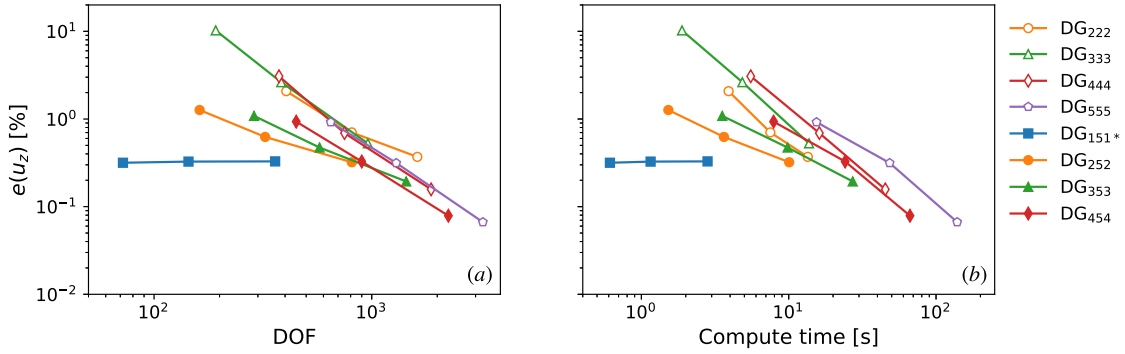


**Fig. 5.** Error in the tip displacement component $u_z$ as a function of (a) the number of degrees of freedom and (b) the compute time for different polynomial approximations in the short beam case.

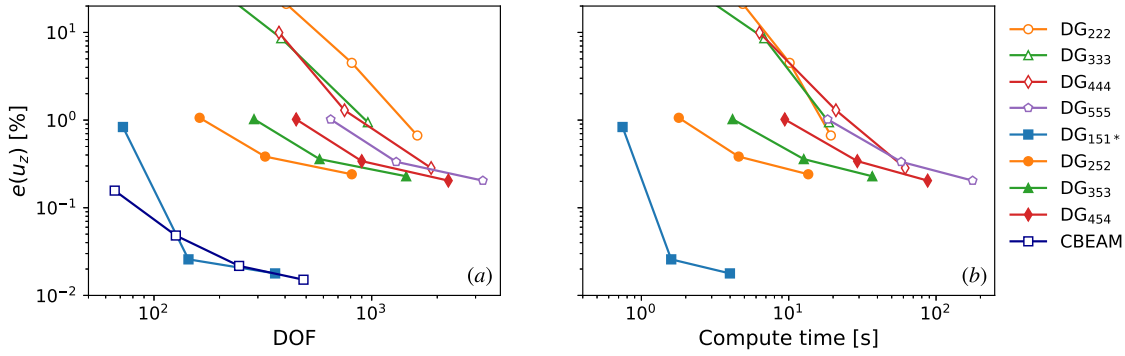


**Fig. 6.** Error in the tip displacement component $u_z$ as a function of (a) the number of degrees of freedom and (b) the compute time for different polynomial approximations in the slender beam case.

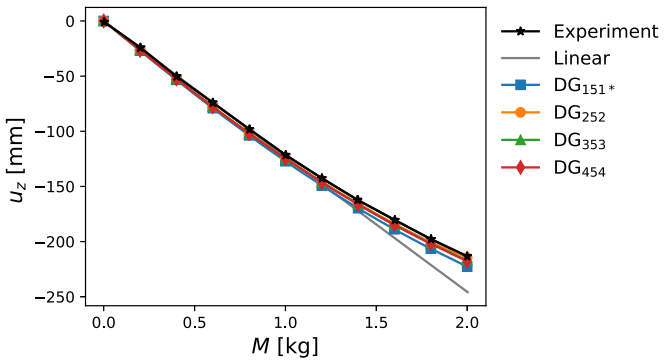


**Fig. 7.** Tip displacement $u_z$ of the Pazy wing during the static structural bending test, for increasing values of the tip mass $M$.

several frameworks and computational tools based on different structural and aerodynamic theories.

The Pazy wing has a semispan $b/2 = 550\,\text{mm}$ and a chord $c = 100\,\text{mm}$ with a NACA0018 airfoil skin made of Oralight. The load-bearing structure of the wing consists of an aluminum spar characterized by width $w_s = 60\,\text{mm}$ and thickness $h_s = 2.25\,\text{mm}$, and centered with respect to the chord. The aluminum spar is characterized by Young's Modulus $E = 71\,\text{GPa}$, Poisson's ratio $\nu = 0.33$ and density $\rho_0 = 2795\,\text{kg/m}^3$. Eventually, the wing structure is complemented by a Nylon 12 internal chassis that provides the aerodynamic shape and supports the skin. The interested reader is referred to Refs. [44–46] for further details regarding the manufactured Pazy wing model.

The first test is similar to the problem considered in the preceding section as it involves a dead load applied at the tip of the wing. The tip displacement $u_z \equiv -u_3(-c/4, b/2, 0)$ is computed as a function of the load tip mass $M$ via the present numerical framework considering different DG schemes and a four-element mesh. The obtained results are reported in Fig. (7) and compared with the experimental values obtained in Refs. [44,45], where the displacements were measured using a motion-capture system based on cameras tracking infrared markers taped onto the wing, while the forces were measured by a force balance.

The comparison shows a discrepancy that is less than 2.1% at the maximum value $M = 2\,\text{kg}$ of the tip load when the $\text{DG}_{454}$ scheme is employed, confirming the accuracy of the present framework. The figure also reports the wing tip displacement computed under the hypothesis of linear elastic behavior, which overestimates the tip displacement by 11.4% when $M = 2\,\text{kg}$.

The second test concerns the aeroelastic response of the Pazy wing. In the experimental campaign described in Refs. [44,45], the wing is mounted vertically in a wind tunnel and its aeroelastic response is measured recording the force component $F_z$, the wing tip displacement $u_z$, and the wing tip twist angle $\theta$ as functions of the dynamic pressure $q \equiv \rho_\infty V_\infty^2/2$ and the angle of attack $\alpha$, considering $\rho_\infty = 1.12\,\text{kg/m}^3$.

The effect of the orders of polynomial approximation, the number of structural elements, and the number of aerodynamic vortices on the computed solution is investigated considering $\alpha = 5°$ and $V_\infty \in [0, 57.5\,\text{m/s}]$. In particular, similar to the computational efficiency analysis performed in Section (4.1), two groups of DG schemes are considered: one group that uses the same order of approximation throughout the wing chord, span and thickness with $p_c = p_b \in \{2, 3, 4, 5\}$, and a second group that uses a mixed-order approach with $p_b = 5$ and $p_c \in \{1, 2, 3, 4\}$;

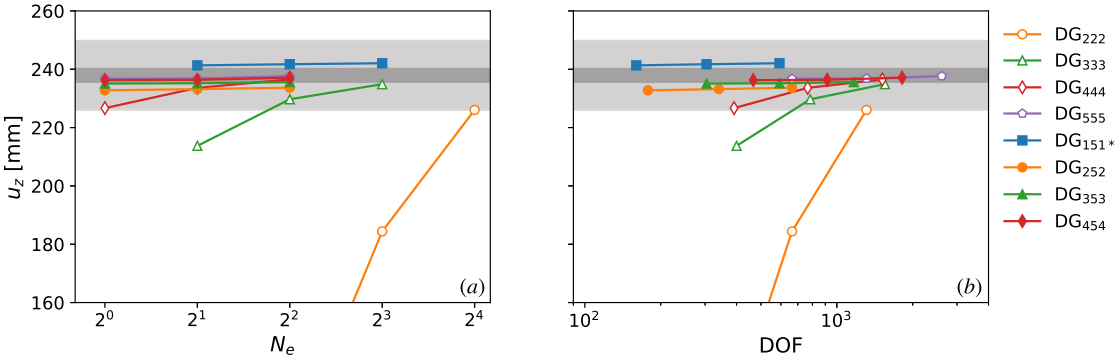


**Fig. 8.** Aeroelastic wing tip displacement as a function of (a) the number of spanwise structural elements and (b) the number of total degrees of freedom. Each curve corresponds to a DG scheme using a different polynomial approximation. The darker and lighter gray areas denote the regions of less than 1% and 5% deviation from the reference value.

in the subsequent figures, the results obtained with the former are displayed using hollow markers, whereas the results obtained with the latter schemes are displayed with filled markers. For each structural discretization, five different aerodynamic meshes consisting of $m_y \times 4m_y$ vortices, with $m_y \in \{2, 4, 8, 16, 32\}$ are considered, where $m_y$ and $4m_y$ are the numbers of vortices along the chord and the span of the wing, respectively; note that, keeping the structural discretization fixed, the solutions obtained using the $8 \times 32$ mesh and the $16 \times 64$ mesh differ from the solution obtained using the $32 \times 128$ mesh by no more than 2% and 0.5%, respectively, for all tested DG schemes, according to the error measure of Eq. (17). It is also worth noting that, for the aeroelastic analyses, the total number of degrees of freedom comprises the structural DOF and the aerodynamic DOF, i.e., $\text{DOF} \equiv 3(1 + p_c)^2(1 + p_b)N_e + N_v$.

Fig. (8a) and (b) report the value of $u_z$ computed at $V_\infty = 57.5\,\text{m/s}$ using the considered DG schemes and the $2 \times 8$ aerodynamic mesh as a function of the number $N_e$ of spanwise structural elements and as a function of the associated DOF, respectively; in the figures, the darker and lighter gray areas denote the regions of less than 1% and 5% deviation from the reference value obtained using an eight-element $\text{DG}_{555}$ scheme. Fig. (8a) shows that DG schemes based on second- and third-order approximations throughout the entire wing structure require four elements and sixteen elements, respectively, to provide an error below 5%, whereas high-order and mixed-order approximations provide a solution within 5% error with one structural element only. In terms of DOF, see Fig. (8b), mixed-order schemes outperform all tested full-order schemes if one considers the 5% error band. This can be observed more clearly in Fig. (9a) and (b), which show the error given in Eq. (17), with $f \equiv u_z$, as a function of DOF and the compute time, respectively. In terms of error-vs-compute time, the one-element mixed-order $\text{DG}_{151*}$, $\text{DG}_{353}$, and $\text{DG}_{454}$ schemes and the one-element $\text{DG}_{555}$ scheme appear to provide the optimal choices among the tested ones. The same error plots are shown for the wing twist angle $\theta$ in Fig. (10); in this case, the discretization choices that offer the optimal error-vs-compute time performance are observed to be the one-element $\text{DG}_{151*}$ scheme, the two- and four-element $\text{DG}_{252}$ schemes, the two- and four-element $\text{DG}_{353}$ schemes, the four-element $\text{DG}_{454}$ scheme, and the two- and four-element $\text{DG}_{555}$ scheme. Compared with the discretizations that are most efficient for wing tip displacement $u_z$, the twist angle is computed more efficiently using a larger number of structural elements. This can be explained by considering that the twist angle is a derivative quantity of the displacement field and is expected to have a slower convergence.

In summary, to achieve the optimal error-vs-DOF and error-vs-compute time trade-offs, the discretizations that are recommended to be combined with a $2 \times 8$ aerodynamic mesh are the mixed-order schemes with two or four structural elements. This has been generally observed for all tested aerodynamic meshes as confirmed in Figs. (11) and (12), which report the error analysis for the wing tip displacement component $u_z$ and for the wing tip twist angle $\theta$, respectively, when a $16 \times 64$ aerodynamic mesh is employed. However, it is observed that the total number of degrees of freedom and the compute time are affected differently by the structural and aerodynamic discretizations. For a coarse aerodynamic mesh, such as the $2 \times 8$ mesh, the number of aerodynamic unknowns $N_v$ is negligible with respect to the structural ones, and the differences in terms of error-vs-DOF and error-vs-compute time are essentially governed by the polynomial approximation employed for the displacement field; see Figs. (9) and (10). Conversely, for a fine aerodynamic mesh, such as the $16 \times 64$ mesh, the aerodynamic degrees of freedom become comparable to or larger than the structural ones, and the differences among the tested DG schemes in terms of error-vs-overall DOF and error-vs-compute time are consequently less evident; see Figs. (11) and (12).

As a final comment on the presented computational efficiency analysis, it is worth noting that, since the problem is nonlinear and is solved via a Newton-Raphson algorithm, the compute time depends also on the set tolerance, which is set to $10^{-7}$ for the present computations. Also, the compute time is not always monotonically increasing with the number of structural mesh elements as a coarser mesh might require more iterations for the residuals to go below the set tolerance.

The results presented in the remaining part of this section are computed considering the $\text{DG}_{151*}$, $\text{DG}_{252}$, $\text{DG}_{353}$, and $\text{DG}_{454}$ schemes, a four-element structural mesh, and a 16×64 VLM grid.

The force component $F_z$, defined as the component along the negative $X_3$ axis, see Fig. (1), of the total aerodynamic force generated by the wing, is reported in Fig. (13) as a function of the dynamic pressure $q$ for three angles of attack, namely $\alpha = 3°$, $\alpha = 5°$, and $\alpha = 7°$. In all cases, a good agreement between the obtained numerical results and the experimental results is observed, with the $\text{DG}_{151*}$ scheme providing a slightly lower aerodynamic force than the other considered DG schemes. The figure also reports the aerodynamic force evaluated under the hypothesis of a linear aeroelastic behavior, showing that nonlinear effects become more pronounced at larger angles of attack.

The results regarding the tip displacement $u_z \equiv -u_3(-c/4, b/2, 0)$ of the wing are reported in Fig. (14). The top, center, and bottom rows of the figure show the results corresponding to the angles of attack $\alpha = 3°$, $\alpha = 5°$, and $\alpha = 7°$, respectively. The left column compares the results obtained via the considered DG schemes with the results obtained via: a geometrically exact beam model coupled with VLM [48], the Modal Rotation Method (MRM) coupled with strip-theory aerodynamics [24], and a nonlinear beam/shell assembly coupled with CFD [46], which are labeled in the figure as Beam + VLM, MRM + Strip theory, Beam/Shell + CFD, respectively. The comparison shows a good agreement between the results obtained via the present methodology and the results obtained

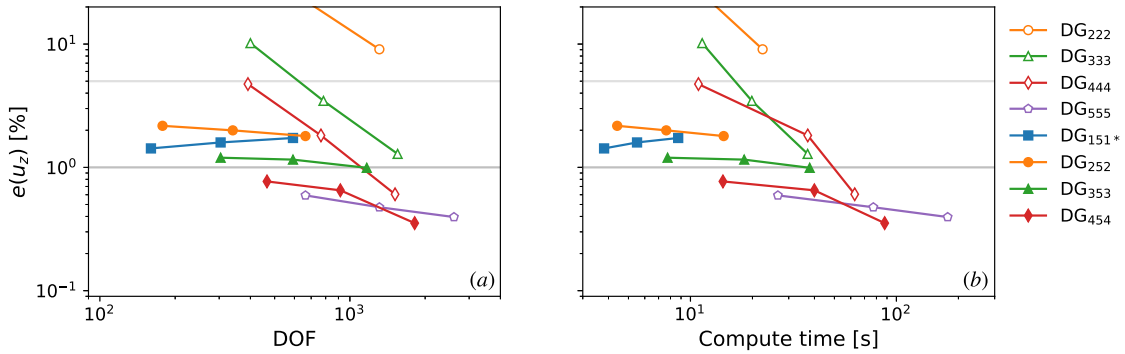


**Fig. 9.** Error in the tip displacement component $u_z$ as a function of (a) the number of degrees of freedom and (b) the compute time for different polynomial approximations in the Pazy wing case using a $2 \times 8$ aerodynamic mesh.

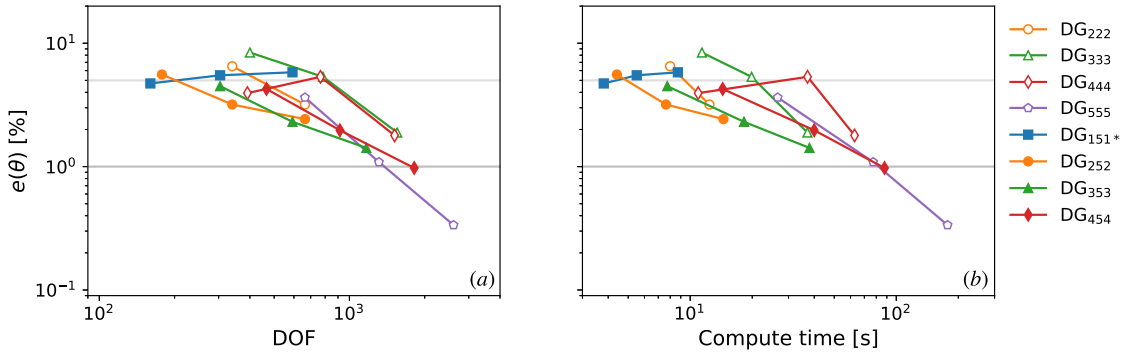


**Fig. 10.** Error in the tip twist angle $\theta$ as a function of (a) the number of degrees of freedom and (b) the compute time for different polynomial approximations in the Pazy wing case using a $2 \times 8$ aerodynamic mesh.

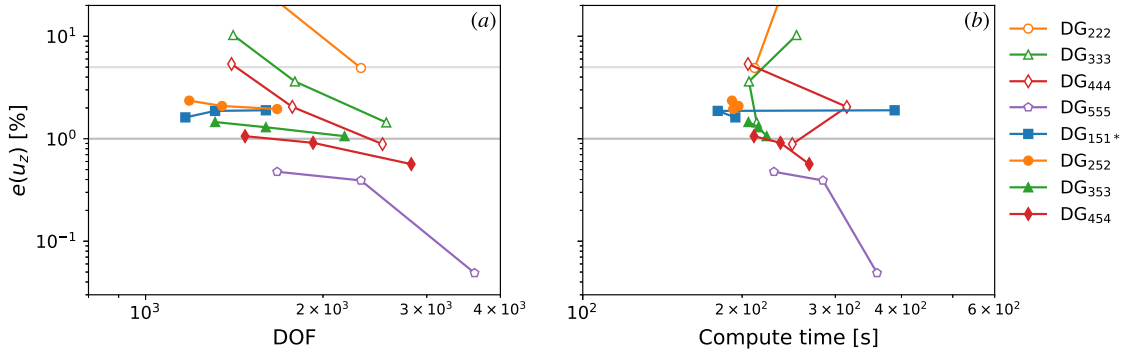


**Fig. 11.** Error in the tip displacement component $u_z$ as a function of (a) the number of degrees of freedom and (b) the compute time for different polynomial approximations in the Pazy wing case using a $16 \times 64$ aerodynamic mesh.

in the literature, with the observed differences attributable to both the different structural models and the different aerodynamic models employed. Additionally, it is worth noting that, for $\alpha = 3°$, the literature models provide similar results, estimating a slightly stiffer structural behavior than that predicted by the present formulation; on the other hand, for $\alpha = 7°$, the results provided by the MRM and beam/shell assembly models appear more in agreement with the results obtained via the present formulation and further away from the results associated with the beam model. Such an observation suggests that the discrepancies in the results computed with different models may be affected by the magnitude of the nonlinear effects. The right column of Fig. (14) shows the comparison between the different structural models and the experimental results available from Refs. [44,45]; it can be seen that the model developed with the present framework estimates a nonlinear aeroelastic response that matches well the experimental data, especially considering the results provided by linear aeroelasticity. Eventually, the insets in the plots reported in the left column of Fig. (14) show to scale the deformed structural and aerodynamic meshes obtained with the present framework at $q = 1851.5$ Pa.

To conclude this section on the analysis of the Pazy wing response, Fig. (15a) and (b) show the local angle of attack $\alpha + \theta$ at the wing tip as a function of the geometrical angle of attack $\alpha$ for $V_\infty = 15$ m/s and $V_\infty = 50$ m/s, respectively. The comparison with the experimental results available in Ref. [45] confirms the accuracy of the presented

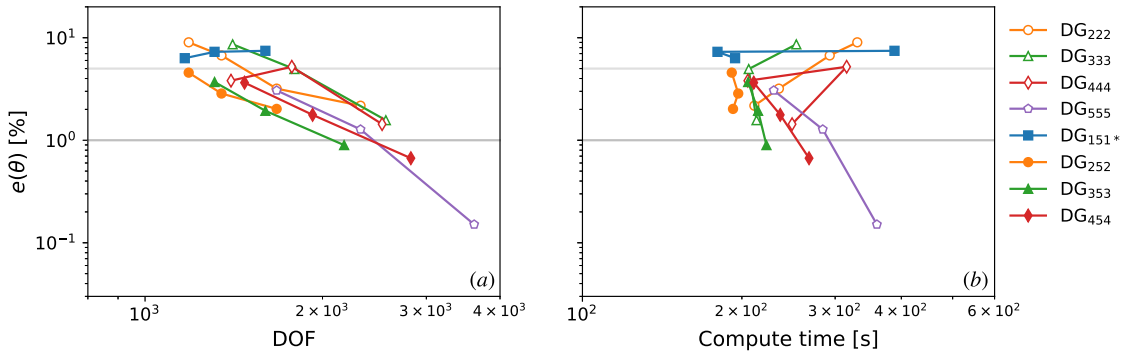


**Fig. 12.** Error in the tip twist angle $\theta$ as a function of (a) the number of degrees of freedom and (b) the compute time for different polynomial approximations in the Pazy wing case using a $16 \times 64$ aerodynamic mesh.

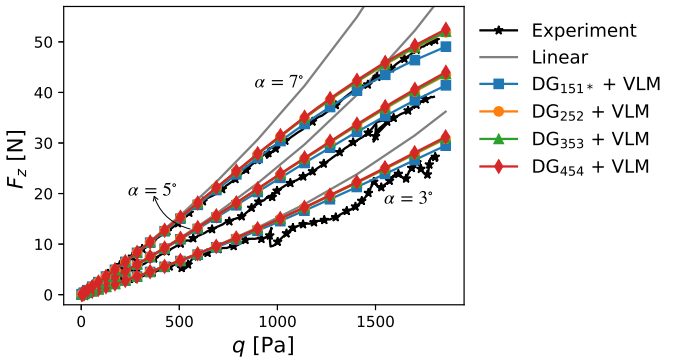


**Fig. 13.** Component along the negative $X_3$ axis, see Fig. (1), of the aerodynamic force generated by the Pazy wing as a function of the dynamic pressure $q$ and the angle of attack $\alpha$.

methodology. Also, as the local angle of attack remains below 10°, it is possible to assume that the hypotheses of small local angles of attack and attached flow required by the VLM formulation remain valid.

### 4.3. Aeroelastic analysis of the Beihang University wing

The last set of tests involves the analysis of the highly flexible wing investigated both experimentally and numerically by the Aeroelasticity Research Branch of the Beihang University, see Ref. [49] The wing features a NACA0015 airfoil and a rectangular planform, with semispan $b/2 = 487\,\text{mm}$ and aerodynamic chord $c = 60\,\text{mm}$. The wing is oriented at an angle of attack $\alpha = 0.4°$ and subject to a free-stream flow characterized by density $\rho_\infty = 1.040\,\text{kg/m}^3$. The structural stiffness of the wing is provided by a slender spar with a rectangular cross section that is centered with respect to the chord and has width $w_s = 7.03\,\text{mm}$ and thickness $h_s = 1.14\,\text{mm}$. The spar is made of an isotropic material with Young's Modulus $E = 230\,\text{GPa}$, Poisson's ratio $\nu = 0.33$ and density $\rho_0 = 7600\,\text{kg/m}^3$. The weight of the wing and a tip mass of $M = 31.5\,\text{g}$ are also included into the calculations.

The displacement $u_z \equiv -u_3(-c/4, b/2, 0)$ is computed as a function of the free-stream velocity $V_\infty$ with the present framework considering different DG schemes, a four-element structural mesh, and $8 \times 64$ VLM mesh. Also in this case, note that the aerodynamic discretization matches the VLM grid reported in Ref. [49]. The obtained results are reported in Fig. (16), showing that the tip displacement computed via the $DG_{353}$ scheme matches well with the numerical values provided in Ref. [49], where a beam structural model coupled to a non-planar VLM aerodynamic model is employed to evaluate the aeroelastic response. Fig. (16b) highlights some differences between the numerical data and the experimental data, also provided in Ref. [49]; however, as commented by the authors of the experimental tests in a different paper, see Ref. [50], such differences might be related to system measurement errors. The wing tip local angle of attack $\alpha + \theta$ is reported as a function of the free-stream velocity $V_\infty$ in Fig. (17); the obtained curve matches the single numerical value provided in Ref. [49]. Also in the case of the Beihang University wing, it is possible to assume that the hypotheses of the VLM formulation remain valid throughout the deformation of the wing as the local angle of attack remains below 4°.

As an additional comment on the present framework, Fig. (16a) also shows that the $DG_{151*}$ and $DG_{252}$ schemes provide instead a stiffer response than the $DG_{353}$ scheme when $V_\infty$ is larger than approximately 25 m/s. This may appear in contrast to the accuracy of different DG schemes observed for the Pazy wing test case. However, it is worth noting that, for the Beihang University wing, the maximum value of the considered free-stream velocity is $V_\infty = 37.5\,\text{m/s}$, which corresponds to approximately 105% of the divergence speed $V_D = 35.8\,\text{m/s}$ of the wing. On the other hand, for the Pazy wing, the maximum value of the considered free-stream velocity is $V_\infty = 57.5\,\text{m/s}$, which corresponds to approximately 60% of the divergence speed $V_D = 95.8\,\text{m/s}$ of the wing at $\alpha = 7°$. Therefore, considering the ratio between the free-stream velocity $V_\infty$ and the divergence speed $V_D$ of the wing as an indicator of the severity of the nonlinear structural effects, these observations also suggest that the differences in the results obtained by different models or numerical approximations become more evident as the contribution of nonlinear terms to the response becomes larger.

Eventually, Fig. (18a), (b), and (c) show to scale the deformed structural and aerodynamic meshes at $V_\infty = 20\,\text{m/s}$, $V_\infty = 30\,\text{m/s}$, and $V_\infty = 37.5\,\text{m/s}$, highlighting the effect of the weight at low speed and the large displacements at high speed.

## 5. Discussion and further developments

This contribution presents a novel computational framework for static aeroelastic analysis of highly flexible wings. The framework is based on the combined use of the discontinuous Galerkin method for solving finite-strain elasticity with variable order of accuracy and the non-planar Vortex Lattice Method for solving potential-flow aerodynamics over a deforming structure.

The capabilities of the framework have been assessed by considering several elastic and aeroelastic test cases and by comparing the obtained results against analytical, computational and experimental data available in the literature. The comparison has confirmed the accuracy of the proposed methodology, showing that a mixed-order of approximation of the displacement field provides a superior computational performance in terms of accuracy-vs-degrees of freedom and accuracy-vs-compute

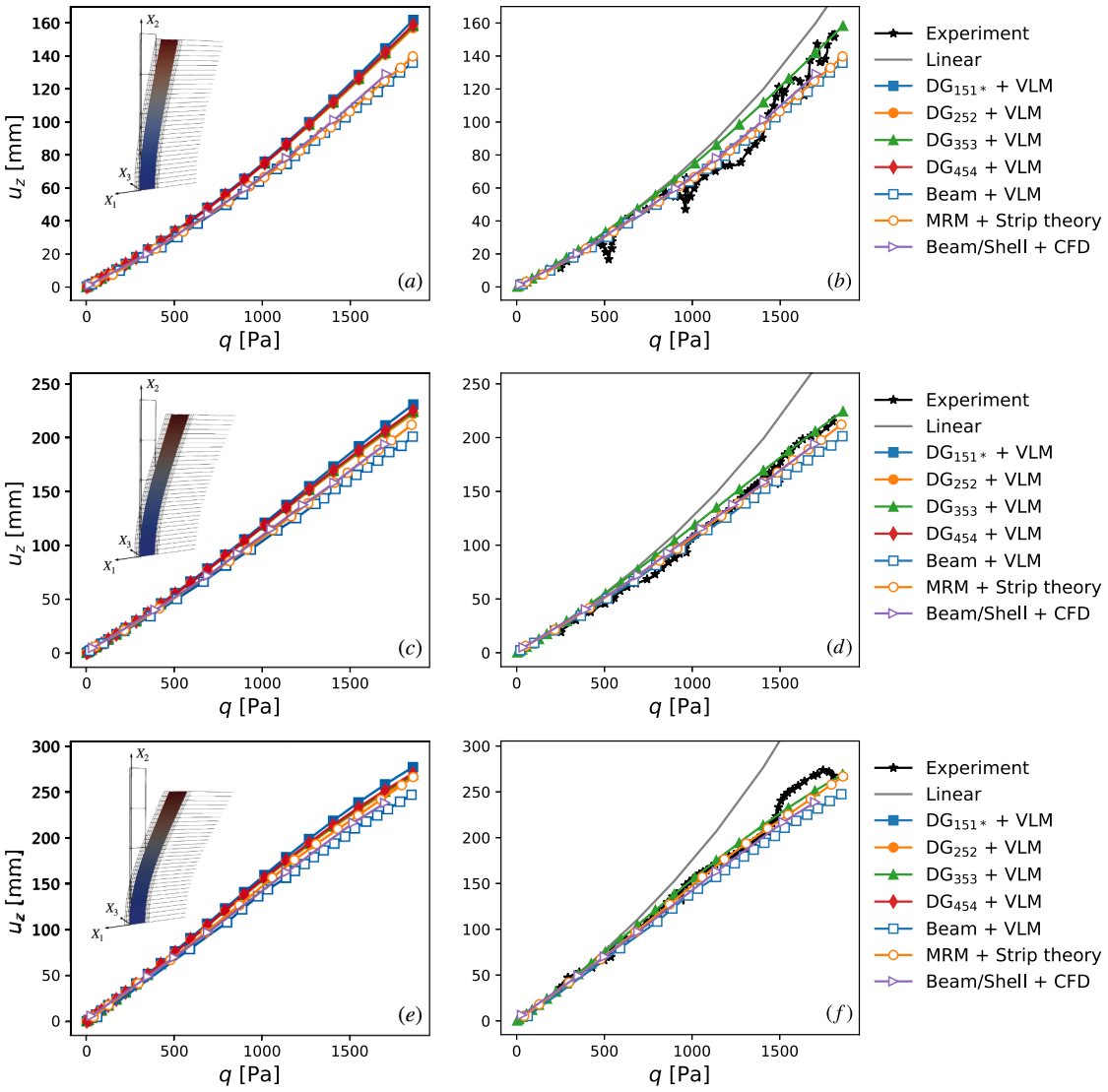


**Fig. 14.** Wing tip displacement $u_z$ of the Pazy wing as a function of the dynamic pressure $q$. The top, center, and bottom rows show the results corresponding to the angles of attack $\alpha = 3°$, $\alpha = 5°$, and $\alpha = 7°$, respectively. The left column compares between different numerical models. The right column compares numerical and experimental results.

time with respect to using the same order of approximation along the three spatial directions. On the other hand, the framework is currently limited to the analysis of an isolated, highly flexible wing with relatively simple geometry, load-bearing internal structure and constitutive law, which undergoes nonlinear static deformations driven by concentrated forces, self-weight and the loads of an incompressible, inviscid and irrotational steady flow. Therefore, several avenues of further research can be identified.

Starting from the fluid perspective, it is worth noting that, as the VLM solves potential-flow aerodynamics, offering similar performance with other potential-flow approaches such as the DLM [29,30], the results obtained by the present approach remain valid for high-Reynolds-number, fully attached steady incompressible flow. The VLM could then be replaced by higher-fidelity tools, such as CFD, which would broaden the range of validity of the aerodynamic solver, allowing nonlinear effects, such as stall, compressibility effects, such as shock waves, or low-Reynolds-number effects to be properly captured. However, the use of CFD is also expected to require significantly longer computational time than VLM to provide the aerodynamic solution; therefore, a parallel direction of further research can be that of modifying the VLM formulation [51,52] or use CFD-based reduced-order models [53] to account for said aerodynamic effects at a lower computational cost.

From the structure perspective, it is worth noting that the present framework has been tested considering wings with unswept rectangular planforms and symmetric airfoil cross sections. Therefore, it would be interesting to investigate how geometrical features such as spanwise-varying, non-symmetric airfoils, the sweep and dihedral angles, or the presence of winglets, would affect the aeroelastic behavior in the finite-strain regime; see for example Ref. [54] as a recent study focusing on the effect of the sweep angle. It is noted that these effects can be captured within the present VLM-based approach, as a swept wing made of non-symmetric, spanwise-varying airfoils can be analyzed by placing the undeformed lattice of vortices over the swept and curved surface identified by the camber curves of the airfoils rather than their chords; see Ref. [55] as an example of a curved VLM for the analysis of hydrofoils without considering hydro-elastic effects. Similarly, the load-bearing structures considered in the present study consist of prismatic spars with rectangular cross-sections, which are relatively simple compared to the internal architecture of general aircraft wings. The presented methodology can be then extended to include elements such as stringers, skin panels and ribs, whose assembly can be realized in a weak sense via the

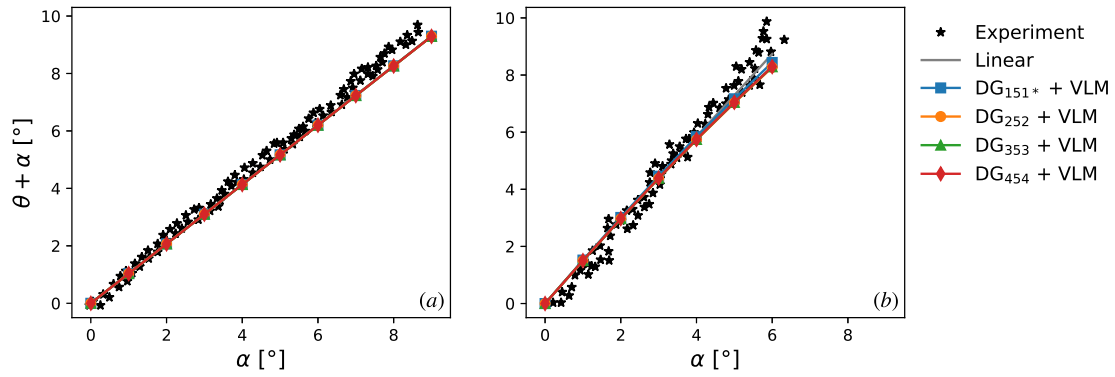


**Fig. 15.** Local angle of attack $\alpha + \theta$ at the wing tip of the Pazy wing as a function of the geometrical angle of attack $\alpha$ for (a) $V_\infty = 15\,\mathrm{m/s}$ and (b) $V_\infty = 50\,\mathrm{m/s}$.

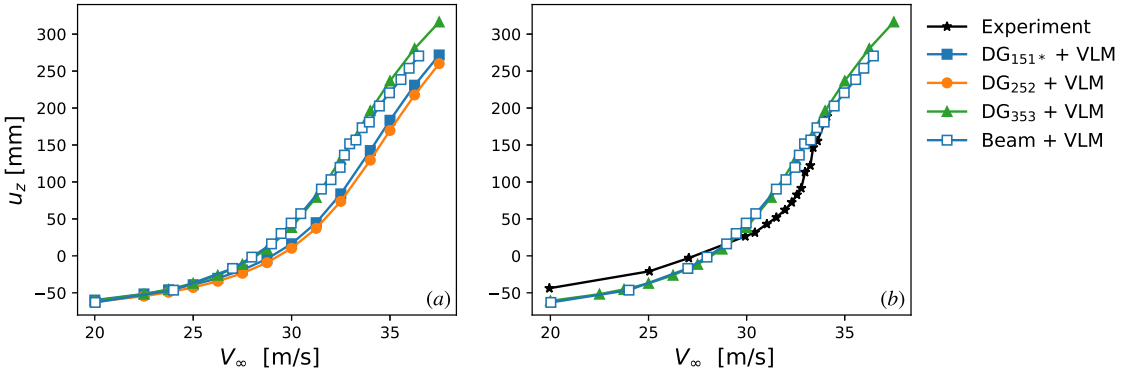


**Fig. 16.** Wing tip displacement $u_z$ of the Beihang University wing as a function of the free-stream velocity $V_\infty$. (*a*) Comparison between different structural models. (*b*) Comparison with experimental measurements.

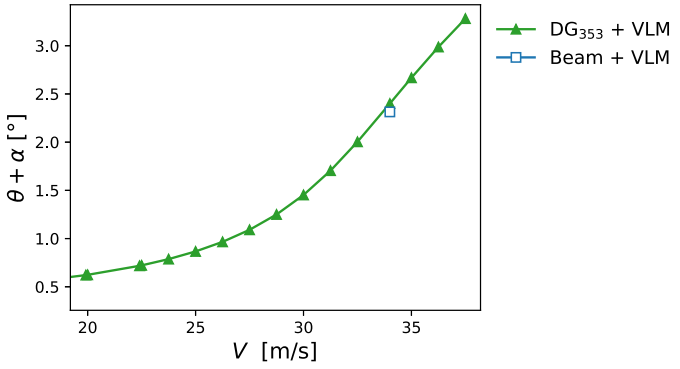


**Fig. 17.** Local angle of attack $\alpha + \theta$ at the wing tip of the Beihang University wing as a function of the free-stream velocity $V_\infty$.

boundary terms that are typical of the DG formulation, see Eq. (10), instead of relying on a high-quality mesh and the node equivalence that are generally needed for a FEM-based approach. Additionally, the DG approach allows introducing complex geometrical features such as cutouts via an immersed boundary approach [56,57] that further simplifies the meshing phase without sacrificing the accuracy of the results. The present formulation can also be extended to account for anisotropic material behaviors stemming, for example, from the use of multilayered composite laminated featuring straight or variable-angle fibers. In such cases, suitable expressions of strain energy function must be considered; see, e.g., Ref. [58]. Regarding the constitutive law, it is also worth noting that different strain energy functions should be considered even for isotropic material behaviors if the load-bearing structures were not metallic and subject to extremely large deformations.

Eventually, as the considered test cases involve static aeroelastic response, a natural extension of the present framework is to consider unsteady aerodynamics and finite-strain elastodynamics, which would allow the study of phenomena such as limit-cycle oscillations [59], the effect of large deformations on flutter boundaries [48], or the gust response of highly flexible wings [60] or wind turbine blades [61,62]. It is worth noting that the framework already allows unsteady aerodynamic and small-strain aeroelastic analyses, see Ref. [28,30]; however, to achieve time-domain aeroelastic capabilities in the finite-strain regime, the framework needs to be extended with a finite-strain elastodynamic solver and with the coupling of such a structural solver with the unsteady aerodynamics solver. In addition, considering time-dependent problems in combination with the aeroelastic response of multiple lifting and non-lifting structures will allow the framework to investigate the flight dynamics performance of highly flexible aircraft [6,63,64] with multi-body effects [65]. Also in such a case, the use of a DG approach would facilitate the coupling between different structural parts and the choice of the approximation space of each part.

Finally, as the proposed methodology relies on the introduction of a penalty parameter $\mu$ to define the numerical fluxes given in Eq. (8) that may depend on the specific application and on the local severity of the elastic nonlinearities, it is worth mentioning that penalty-free DG formulations, see, e.g., Ref. [66,67], could also be integrated into the present framework to circumvent the need for such a parameter.

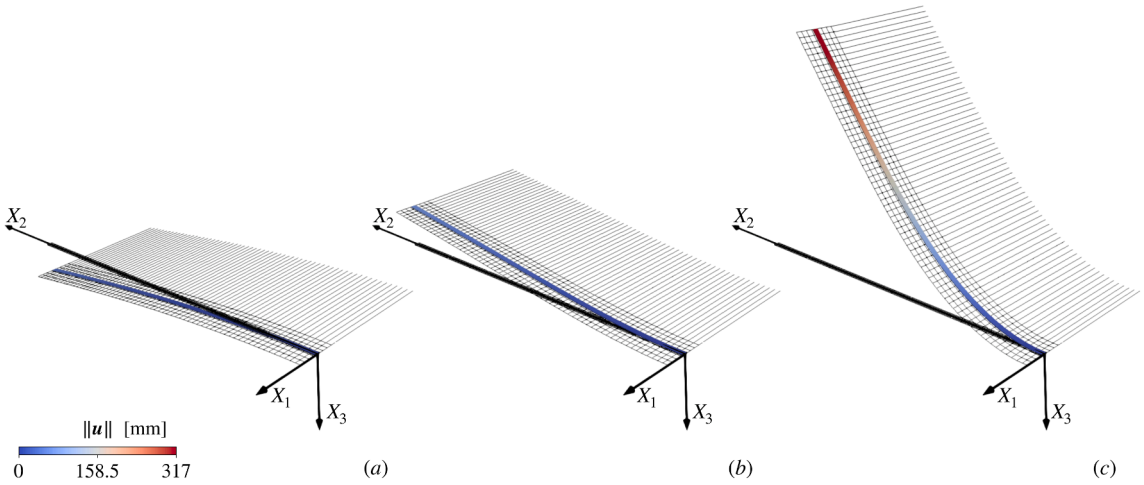


**Fig. 18.** Deformed structural and aerodynamic meshes of the Beihang University wing corresponding to (*a*) $V_\infty = 20\,\mathrm{m/s}$, (*b*) $V_\infty = 30\,\mathrm{m/s}$, and (*c*) $V_\infty = 37.5\,\mathrm{m/s}$.

## 6. Conclusion

This research study presents, for the first time, a computational framework for finite-strain static aeroelasticity based on the combined use of the discontinuous Galerkin method and the non-planar Vortex Lattice Method. The DG-based structural solver provides flexibility in the choice of the approximation space employed for the displacement field, allowing seamless testing of different approximation orders to solve the finite-strain, total Lagrangian elasticity equations. On the other hand, the non-planar VLM is a fast computational tool for evaluating the aerodynamic forces on the deformed structure.

The proposed formulation has been developed, implemented, and validated through a series of elastic and aeroelastic tests involving highly flexible wings. The obtained results have been compared with reference data from the literature, including both experimental measurements and computational approaches based on various aerodynamic and structural coupled models. The comparison highlights the influence of different modeling choices or approximations on the aeroelastic response, and demonstrates the accuracy and effectiveness of the developed framework.

## CRediT authorship contribution statement

**Elisa Testaquatra:** Writing – review & editing, Writing – original draft, Visualization, Validation, Software, Methodology, Investigation, Data curation; **Vincenzo Gulizzi:** Writing – review & editing, Writing – original draft, Validation, Supervision, Software, Project administration, Methodology, Funding acquisition, Formal analysis, Conceptualization.

## Declaration of competing interest

The authors declare that they have no known competing financial interests or personal relationships that could have appeared to influence the work reported in this paper.

## Acknowledgments

VG acknowledges the support by the European Union–Next Generation EU - PNRR M4 - C2 - investimento 1.1: Fondo per il Programma Nazionale di Ricerca e Progetti di Rilevante Interesse Nazionale (PRIN) - PRIN 2022 cod.2022AALLEC dal titolo “Hydrodynamic devices for micro-particle trapping and vibrational energy harvesting (HYDRA)” CUP B53D23005770006.

## Data availability

Data will be made available on request.

## References

[1] F. Afonso, J. Vale, É. Oliveira, F. Lau, A. Suleman, A review on non-linear aeroelasticity of high aspect-ratio wings, Prog. Aerosp. Sci. 89 (2017) 40–57.
[2] D.H. Hodges, A mixed variational formulation based on exact intrinsic equations for dynamics of moving beams, Int. J. Solids Struct. 26 (11) (1990) 1253–1273.
[3] M. Patil, D. Hodges, C. Cesnik, Nonlinear aeroelastic analysis of aircraft with high-aspect-ratio wings, in: 39th AIAA/ASME/ASCE/AHS/ASC Structures, Structural Dynamics, and Materials Conference and Exhibit, 1998, p. 1955.
[4] M.J. Patil, D.H. Hodges, C.E.S. Cesnik, Nonlinear aeroelasticity and flight dynamics of high-altitude long-endurance aircraft, J. Aircr. 38 (1) (2001) 88–94.
[5] M. Smith, M. Patil, D. Hodges, CFD-based analysis of nonlinear aeroelastic behavior of high-aspect ratio wings, in: 19th AIAA Applied Aerodynamics Conference, 2001, p. 1582.
[6] J. Murua, R. Palacios, J.M.R. Graham, Applications of the unsteady vortex-lattice method in aircraft aeroelasticity and flight dynamics, Prog. Aerosp. Sci. 55 (2012) 46–72.
[7] C.M. Shearer, C.E.S. Cesnik, Nonlinear flight dynamics of very flexible aircraft, J. Aircr. 44 (5) (2007) 1528–1545.
[8] W. Su, C.E.S. Cesnik, Strain-based geometrically nonlinear beam formulation for modeling very flexible aircraft, Int. J. Solids Struct. 48 (16–17) (2011) 2349–2360.
[9] W. Su, C.E.S. Cesnik, Strain-based analysis for geometrically nonlinear beams: a modal approach, J. Aircr. 51 (3) (2014) 890–903.
[10] D.H. Hodges, Geometrically exact, intrinsic theory for dynamics of curved and twisted anisotropic beams, AIAA J. 41 (6) (2003) 1131–1137.
[11] R. Palacios, Nonlinear normal modes in an intrinsic theory of anisotropic beams, J. Sound Vib. 330 (8) (2011) 1772–1792.
[12] R. Palacios, A. Cea, Nonlinear modal condensation of large finite element models: application of Hodges’s intrinsic theory, AIAA J. 57 (10) (2019) 4255–4268.
[13] A. Cea, R. Palacios, A non-intrusive geometrically nonlinear augmentation to generic linear aeroelastic models, J. Fluids Struct. 101 (2021) 103222.
[14] A. Cea, R. Palacios, Geometrically nonlinear effects on the aeroelastic response of a transport aircraft configuration, J. Aircr. 60 (1) (2023) 205–220.
[15] C. de Souza, R.G. da Silva, C. Cesnik, Nonlinear aeroelastic framework based on vortex-lattice method and corotational shell finite element, in: 53rd AIAA/ASME/ASCE/AHS/ASC Structures, Structural Dynamics and Materials Conference 20th AIAA/ASME/AHS Adaptive Structures Conference 14th AIAA, 2012, p. 1976.
[16] N. Tsushima, T. Yokozeki, W. Su, H. Arizono, Geometrically nonlinear static aeroelastic analysis of composite morphing wing with corrugated structures, Aerosp. Sci. Technol. 88 (2019) 244–257.
[17] N. Tsushima, M. Tamayama, H. Arizono, K. Makihara, Geometrically nonlinear aeroelastic characteristics of highly flexible wing fabricated by additive manufacturing, Aerosp. Sci. Technol. 117 (2021) 106923.
[18] S. Qiao, H. Gao, Y. Lyu, L. Hua, F. Wang, Nonlinear aeroelastic characteristics analysis of composite wing with high aspect ratio based on co-rotational method, J. Fluids Struct. 82 (2018) 619–637.
[19] A.C. Gray, G.J. Kennedy, J.R. Martins, Geometrically nonlinear high-fidelity aerostructural optimization for highly flexible wings, Struct. Multidiscip. Optim. 69 (1) (2026) 6.
[20] X. Ai, Y. Bai, W. Qian, Y. Li, X. Chen, Aeroelastic investigation on an all-movable horizontal tail with free-play nonlinearity, J. Low Freq. Noise Vib. Act. Control 43 (2) (2024) 634–650.

[21] X. Ai, Y. Bai, X. Chen, J. Liu, Z. Chen, Q. Yu, W. Qian, Nonlinear aeroelastic analysis of an all-movable horizontal tail with bending free-play, Aerosp. Sci. Technol. (2025) 111339.
[22] R.R. Medeiros, C.E.S. Cesnik, E.B. Coetzee, Computational aeroelasticity using modal-based structural nonlinear analysis, AIAA J. 58 (1) (2020) 362–371.
[23] A. Drachinsky, D.E. Raveh, Modal rotations: a modal-based method for large structural deformations of slender bodies, AIAA J. 58 (7) (2020) 3159–3173.
[24] A. Drachinsky, D.E. Raveh, Nonlinear aeroelastic analysis of highly flexible wings using the modal rotation method, AIAA J. 60 (5) (2022) 3122–3134.
[25] A. Varello, E. Carrera, L. Demasi, Vortex lattice method coupled with advanced one-dimensional structural models, J. Aeroelasticity Struct. Dyn. 2 (2) (2011) 53–78.
[26] E. Carrera, A. Varello, L. Demasi, A refined structural model for static aeroelastic response and divergence of metallic and composite wings, CEAS Aeronaut. J. 4 (2) (2013) 175–189.
[27] V. Gulizzi, I. Benedetti, Computational aeroelastic analysis of wings based on the structural discontinuous Galerkin and aerodynamic vortex lattice methods, Aerosp. Sci. Technol. 144 (2024) 108808.
[28] F. Montano, D. Campagna, I. Dimino, V. Gulizzi, I. Benedetti, A discontinuous Galerkin framework for aeroelastic flutter analysis with variable-order structural modeling capability, Mech. Adv. Mater. Struct. 33 (1) (2025) 1–18.
[29] D. Campagna, V. Gulizzi, I. Benedetti, A DG-VLM framework for computational static aeroelastic analysis of composite wings, Compos. Struct. 353 (2025) 118697.
[30] D. Campagna, I. Benedetti, V. Gulizzi, Variable-order framework for aeroelastic flutter analysis of laminated composite wings, Compos. Struct. 371 (2025) 119508.
[31] M. Grifò, A. Da Ronch, I. Benedetti, A computational aeroelastic framework based on high-order structural models and high-fidelity aerodynamics, Aerosp. Sci. Technol. 132 (2023) 108069.
[32] M. Grifò, V. Gulizzi, A. Milazzo, A. Da Ronch, I. Benedetti, High-fidelity aeroelastic transonic analysis using higher-order structural models, Compos. Struct. 321 (2023) 117315.
[33] T. Belytschko, W.K. Liu, B. Moran, K. Elkhodary, Nonlinear Finite Elements for Continua and Structures, John wiley & sons, 2014.
[34] M.E. Gurtin, E. Fried, L. Anand, The Mechanics and Thermodynamics of Continua, Cambridge university press, 2010.
[35] J. Katz, A. Plotkin, Low-Speed Aerodynamics, 13, Cambridge university press, 2001.
[36] J.J. Bertin, R.M. Cummings, Aerodynamics for Engineers, Cambridge University Press, 2021.
[37] V. Gulizzi, I. Benedetti, A. Milazzo, High-order accurate beam models based on discontinuous Galerkin methods, Aerotec. Missili Spaz. 102 (4) (2023) 293–308.
[38] V. Gulizzi, I. Benedetti, A. Milazzo, High-order accurate transient and free-vibration analysis of plates and shells, J. Sound Vib. 587 (2024) 118479.
[39] L. Yuan, C.-W. Shu, Discontinuous Galerkin method based on non-polynomial approximation spaces, J. Comput. Phys. 218 (1) (2006) 295–323.
[40] D.N. Arnold, F. Brezzi, B. Cockburn, L.D. Marini, Unified analysis of discontinuous Galerkin methods for elliptic problems, SIAM J. Numer. Anal. 39 (5) (2002) 1749–1779.
[41] L. Noels, R. Radovitzky, A general discontinuous Galerkin method for finite hyperelasticity. formulation and numerical applications, Int. J. Numer. Methods Eng. 68 (1) (2006) 64–97.
[42] K.E. Bisshopp, D.C. Drucker, Large deflection of cantilever beams, Q. Appl. Math. 3 (3) (1945) 272–275.
[43] A. Pagani, R. Augello, E. Carrera, Frequency and mode change in the large deflection and post-buckling of compact and thin-walled beams, J. Sound Vib. 432 (2018) 88–104.
[44] O. Avin, D.E. Raveh, A. Drachinsky, Y. Ben-Shmuel, M. Tur, An experimental benchmark of a very flexible wing, in: AIAA Scitech 2021 Forum, 2021, p. 1709.
[45] O. Avin, D.E. Raveh, A. Drachinsky, Y. Ben-Shmuel, M. Tur, Experimental aeroelastic benchmark of a very flexible wing, AIAA J. 60 (3) (2022) 1745–1768.
[46] M. Ritter, J. Hilger, A. Ribeiro, A.E. Öngüt, M. Righi, D.E. Raveh, L.G.P. dos Santos, A. Drachinsky, C. Riso, C.E. Cesnik, et al., Collaborative Pazy wing analyses for the third aeroelastic prediction workshop, in: AIAA SciTech 2024 Forum, 2024, p. 0419.
[47] B.K. Stanford, K.E. Jacobson, P. Chwalowski, Aeroelastic analysis of highly flexible wings with linearized frequency-domain aerodynamics, J. Aircr. 61 (2) (2024) 365–374.
[48] N. Goizueta, A. Wynn, R. Palacios, A. Drachinsky, D.E. Raveh, Flutter predictions for very flexible wing wind tunnel test, J. Aircr. 59 (4) (2022) 1082–1097.
[49] C. Xie, L. Wang, C. Yang, Y. Liu, Static aeroelastic analysis of very flexible wings based on non-planar vortex lattice method, Chin. J. Aeronaut. 26 (3) (2013) 514–521.
[50] C. Xie, Y. Liu, C. Yang, J.E. Cooper, Geometrically nonlinear aeroelastic stability analysis and wind tunnel test validation of a very flexible wing, Shock Vib. 2016 (1) (2016) 5090719.
[51] D. Chaparro, G.E. Fujiwara, E. Ting, N.T. Nguyen, Aerodynamic modeling of transonic aircraft using vortex lattice coupled with transonic small disturbance for conceptual design, in: 34th AIAA Applied Aerodynamics Conference, 2016, p. 3418.
[52] M. Parenteau, E. Laurendeau, A transonic, viscous nonlinear frequency domain vortex lattice method for aeroelastic analyses, J. Fluids Struct. 107 (2021) 103406.
[53] K. Li, J. Kou, W. Zhang, Aeroelastic reduced-order modeling for efficient static aeroelastic analysis considering geometric nonlinearity, J. Fluids Struct. 124 (2024) 104055.
[54] B. Revivo, D.E. Raveh, Static aeroelasticity and stability of very flexible swept wings, in: AIAA SCITECH 2025 Forum, 2025, p. 1018.
[55] A. Cirello, V. Gulizzi, A. Mancuso, Vortex lattice method approach to sailing yacht foil design: feasibility and comparison with RANS method results, Int. J. Interact. Des. Manuf. (2025) 1–12. https://link.springer.com/article/10.1007/s12008-025-02378-4
[56] V. Gulizzi, I. Benedetti, A. Milazzo, An implicit mesh discontinuous Galerkin formulation for higher-order plate theories, Mech. Adv. Mater. Struct. 27 (17) (2020) 1494–1508.
[57] G. Guarino, V. Gulizzi, A. Milazzo, High-fidelity analysis of multilayered shells with cut-outs via the discontinuous Galerkin method, Compos. Struct. 276 (2021) 114499.
[58] P. Chiaia, A. Pagani, E. Carrera, Large strain and 3D stress analysis of laminated fiber-reinforced soft material structures with high order beam finite elements, Comput. Struct. 313 (2025) 107735.
[59] M.J. Patil, D.H. Hodges, C.E.S. Cesnik, Limit-cycle oscillations in high-aspect-ratio wings, J. Fluids Struct. 15 (1) (2001) 107–132.
[60] S. Düssler, C. Mertens, R. Palacios, Gust response predictions of a very flexible wing model, J. Aircr. 63 (1) (2026) 303–314.
[61] M.M. Rezaei, M. Behzad, H. Haddadpour, H. Moradi, Aeroelastic analysis of a rotating wind turbine blade using a geometrically exact formulation, Nonlinear Dyn. 89 (4) (2017) 2367–2392.
[62] A.K. Sabale, N.K.V. Gopal, Nonlinear aeroelastic analysis of large wind turbines under turbulent wind conditions, AIAA J. 57 (10) (2019) 4416–4432.
[63] C.-S. Chang, D.H. Hodges, M.J. Patil, Flight dynamics of highly flexible aircraft, J. Aircr. 45 (2) (2008) 538–545.
[64] S. Shafaghat, M.A. Noorian, S. Irani, Nonlinear aeroelastic analysis of a HALE aircraft with flexible components, Aerosp. Sci. Technol. 127 (2022) 107663.
[65] B. Preston, U. Fasel, R. Palacios, A. Castrichini, Multibody simulation of flexible aircraft with variable-sweep wingtips, AIAA J. 64 (2) (2026) 955–968.
[66] J. Jaśkowiec, N. Sukumar, Penalty-free discontinuous Galerkin method, Int. J. Numer. Methods Eng. 125 (12) (2024) e7472.
[67] H. Duan, J. Ma, A penalty-free and essentially stabilization-free DG method for convection-dominated second-order elliptic problems, J. Sci. Comput. 100 (2) (2024) 59.